CrossMark

JFM PAPERS

The rotation of a sedimenting spheroidal particle in a linearly stratified fluid

Arun Kumar Varanasi[1],†, Navaneeth K. Marath[2],† and Ganesh Subramanian[1],†

[1]Engineering Mechanics Unit, Jawaharlal Nehru Center for Advanced Scientific Research, Bangalore 560064, India

[2]Mechanical Engineering, Indian Institute of Technology, Ropar 140001, India

We derive analytically the angular velocity of a spheroid, of an arbitrary aspect ratio κ, sedimenting in a linearly stratified fluid. The analysis demarcates regions in parameter space corresponding to broadside-on and edgewise settling in the limit Re, $Ri_v \ll 1$, where $Re = \rho_0 U L / \mu$ and $Ri_v = \gamma L^3 g / \mu U$, the Reynolds and viscous Richardson numbers, respectively, are dimensionless measures of the importance of inertial and buoyancy forces relative to viscous ones. Here, L is the spheroid semi-major axis, U an appropriate settling velocity scale, μ the fluid viscosity and γ (> 0) the (constant) density gradient characterizing the stably stratified ambient, with the fluid density ρ_0 taken to be a constant within the Boussinesq framework. A reciprocal theorem formulation identifies three contributions to the angular velocity: (1) an $O(Re)$ inertial contribution that already exists in a homogeneous ambient, and orients the spheroid broadside-on; (2) an $O(Ri_v)$ hydrostatic contribution due to the ambient stratification that also orients the spheroid broadside-on; and (3) a hydrodynamic contribution arising from the perturbation of the ambient stratification whose nature depends on Pe; $Pe = U L / D$ being the Péclet number with D the diffusivity of the stratifying agent. For $Pe \ll 1$, this contribution is $O(Ri_v)$ and orients prolate spheroids edgewise for all κ (> 1). For oblate spheroids, it changes sign across a critical aspect ratio $\kappa_c \approx 0.41$, orienting oblate spheroids with $\kappa_c < \kappa < 1$ edgewise and those with $\kappa < \kappa_c$ broadside-on. For $Pe \ll 1$, the hydrodynamic component is always smaller in magnitude than the hydrostatic one, so a sedimenting spheroid in this limit always orients broadside-on. For $Pe \gg 1$, the hydrodynamic contribution is dominant, being $O(Ri_v^{2/3})$ in the Stokes stratification regime characterized by $Re \ll Ri_v^{1/3}$, and orients the spheroid edgewise regardless of κ. Consideration of the inertial and large-Pe stratification-induced angular velocities leads to two critical curves which separate the broadside-on and edgewise settling regimes in the $Ri_v / Re^{3/2}$–κ plane, with the

† Email addresses for correspondence: arun.target@gmail.com, navaneeth@iitrpr.ac.in, sganesh@jncasr.ac.in

region between the curves corresponding to stable intermediate equilibrium orientations. The predictions for large *Pe* are broadly consistent with observations.

1. Introduction

The atmosphere and oceans being, on average, in a stably stratified state, the motion of particles as well as living organisms in a stratified ambient is of obvious importance in natural settings. A large fraction of the research on the vertical motion of particles through stratified fluids, including cases of both sharp (Srdic-Mitrovic, Mohamed & Fernando 1999; Roberto *et al.* 2009) and continuous (Hanazaki 1988; Hanazaki, Konishi & Okamura 2009; Yick *et al.* 2009; Doostmohammadi, Stocker & Ardekani 2012; Doostmohammadi, Dabiri & Ardekani 2014; Mehaddi, Candelier & Mehlig 2018) stratification profiles, has, however, focused on spherical particles. Although this research has shed light on the non-trivial effects of stratification on the structure of the disturbance flow field induced by a sedimenting sphere, for instance, its sensitive dependence on the diffusivity of the stratifying agent via the Péclet number (*Pe*) (see List 1971; Ardekani & Stocker 2010; Doostmohammadi *et al.* 2012; Varanasi & Subramanian 2021; Shaik & Ardekani 2020), the vast majority of particles and living (micro)organisms in natural scenarios depart from the idealized spherical shape. Indeed, both marine phytoplankton and zooplankton come in an astonishing variety of shapes (Kiorboe 2011; Lab 2018), and there are provocative questions to be addressed with regard to the large-scale effects of zooplankton migration across the oceanic pycnocline (Kunze *et al.* 2006; Visser 2007; Katija & Dabiri 2009; Subramanian 2010; Varanasi & Subramanian 2021). Other classes of organic particles including marine snow aggregates (Prairie *et al.* 2015), phytodetritus and faecal pellets, which make up the so-called biological pump (Turner 2015), and undesired microplastics (Cole *et al.* 2011; Turner & Holmes 2011), also depart significantly from the canonical spherical geometry. Extensive research over a long time has now led to a fairly mature understanding of the dynamics of anisotropic particles sedimenting in a homogeneous ambient (Guillaume & Magnaudet 2002; Auguste, Magnaudet & Fabre 2013). Although the non-trivial effects of unsteady wake dynamics come into play at higher Reynolds numbers (*Re*), as manifest by the onset of path instabilities of sedimenting spheroids (Patricia *et al.* 2012), the simplest scenario which prevails for low to moderate *Re*, when the wake has a quasi-steady character, involves inertial forces acting to turn sedimenting anisotropic particles broadside-on. For small *Re*, and in the case where the anisotropic particle is a prolate or an oblate spheroid, the inertial torque acting to turn the spheroid broadside-on has been determined analytically as a function of the spheroid aspect ratio (Dabade, Marath & Subramanian 2015; Jiang *et al.* 2020). Recent direct numerical simulations (DNS) have shown this inertial torque to strongly influence the orientation distribution of such particles in an ambient turbulent flow (Gustavsson *et al.* 2019; Anand, Ray & Subramanian 2020), with these distributions exhibiting a pronouncedly non-Gaussian character (Anand *et al.* 2020).

The present study is specifically motivated by very recent experiments involving cylindrical and disk-shaped particles (Mrokowska 2018; Mercier *et al.* 2020; Mrokowska 2020*b*,*a*) that are among the first to systematically explore the role of shape anisotropy for sedimenting particles in a heterogeneous stably stratified fluid ambient. The experiments and computations reported by Mercier *et al.* (2020) pertain to a linearly stratified ambient, whereas the experiments reported in Mrokowska (2018), Mrokowska (2020*b*)

and Mrokowska ([2020](#)*a*) pertain to a nonlinearly stratified fluid layer sandwiched between homogeneous upper and lower layers. Although the detailed results obtained for the two sets of experiments differ on account of the differing nature of the ambient stratification, one of the most important findings, common to both sets of experiments, pertains to the ability of the torque due to buoyancy forces to oppose, and even overwhelm the aforementioned inertial torque that acts in a homogeneous setting, thereby turning the particle longside-on. It is worth mentioning here that the rotation of an anisotropic particle (a prolate spheroid of aspect ratio two) towards the edgewise configuration, in a stratified setting, was originally discovered in the numerical simulations of Doostmohammadi & Ardekani ([2014](#)). Such a rotation was found to occur for both a linear and a discontinuous stratification (a density interface). This study of anisotropic particle reorientation was, in turn, motivated by an earlier work, of the same authors, where they found analogous behaviour in the context of pair interactions of sedimenting spherical particles; particle pairs in close contact were found to rotate at a slower rate in a stratified ambient, implying a stratification-induced torque favouring a long-side orientation of the resulting dumbbell-shaped configuration (Doostmohammadi & Ardekani [2013](#)). A recent theoretical study (Dandekar, Shaik & Ardekani [2020](#)) has analytically determined the stratification-induced corrections to the force and torque acting on a non-spherical particle settling in a viscous linearly stratified ambient. Although a correction to the force was determined in terms of the viscous Richardson number (Ri_v defined in § [2](#)) for both chiral and achiral particles, a hydrodynamic torque was found to arise from buoyancy forces only for chiral particles, the origin of this torque being the translation–rotation coupling that already exists for such particles in a homogeneous ambient. As shown later, the hydrodynamic torque for the spheroids (achiral particles) considered here arises at an order higher than that explored in the previous study. Thus, the said analysis does not explain one of the principal observations in the aforementioned experiments and simulations involving the stratification-induced transition of a sedimenting anisotropic but achiral particle from a broadside-on to an edgewise configuration.

In the present study, we show that buoyancy forces associated with the ambient stratification do lead to a torque even for achiral particles modelled as prolate and oblate spheroids of an arbitrary aspect ratio. This stratification-induced torque consists of both hydrostatic and hydrodynamic components; the former contribution has been given in Dandekar *et al.* ([2020](#)) for a slender cylindrical rod of a circular cross-section, and acts to orient the rod broadside-on. Consistent with this finding, it is shown here that the hydrostatic contribution turns a spheroid broadside-on regardless of whether its prolate or oblate, and regardless of its aspect ratio. More importantly, however, the hydrodynamic component of the stratification-induced torque is shown to be asymptotically larger than the hydrostatic one for large *Pe*, and orients spheroids edgewise, thereby offering the first theoretical explanation of the experimental observations above: that of edgewise settling of an anisotropic particle in a stratified fluid.

The layout of the paper is as follows. In § [2](#), we describe the reciprocal theorem formulation which yields the angular velocity of a spheroid sedimenting in a linearly stratified viscous fluid in terms of distinct contributions originating from the effects of fluid inertia and the buoyancy forces associated with the ambient stratification. The angular velocity contributions arising from the fluid inertial torque, and the hydrostatic component of the stratification torque, are readily evaluated on account of their regular character, and this calculation is given in § [3](#). The calculation of the hydrodynamic component of the stratification torque is more involved, being sensitively dependent on *Pe*, and is carried out in §§ [4.1](#) and [4.2](#) in the limits *Pe* ≪ 1 and *Pe* ≫ 1, respectively. Certain subtle aspects

pertaining to the low-*Pe* regime are discussed in § 4.1.1 and in Appendix B; specifically, the derivation of an outer-region torque contribution in the latter appendix helps demarcate the regime of validity of the analysis in § 4.1. Finally, § 5 discusses the transition from broadside-on to edgewise settling that arises due to the competing influences of the inertial and hydrodynamic components of the stratification torque, at large *Pe*, and ends with a qualitative comparison with recent experiments. In § 6, we briefly indicate possible lines of investigation for the future.

2. A sedimenting spheroid in a linearly stratified ambient: the generalized reciprocal theorem formulation

The torque acting on a spheroid, sedimenting in a stably stratified fluid ambient, is derived in the following using the generalized reciprocal theorem (see Kim & Karrila 1991; Dabade *et al.* 2015; Dabade, Marath & Subramanian 2016). The theorem relates two pairs of stress and velocity fields, and may be stated in the form:

$$\int_{S_p} \sigma_{ij}^{(2)} u_i'^{(1)} n_j \, \mathrm{d}S - \int_{S_p} \sigma_{ij}^{(1d)} u_i^{(2)} n_j \, \mathrm{d}S = \int \frac{\partial \sigma_{ij}^{(1d)}}{\partial x_j} u_i^{(2)} \, \mathrm{d}V, \qquad (2.1)$$

where S_p denotes the surface of the spheroid, and with the neglect of the surface integrals at infinity, the volume integral on the right-hand side of (2.1) is over the unbounded fluid domain external to the spheroid. In (2.1), the pair $(\boldsymbol{\sigma}^{(1d)}, \boldsymbol{u}'^{(1)})$ denotes the dynamic stress and velocity fields associated with the problem of interest, namely a torque-free spheroid sedimenting under gravity in an ambient linearly stratified medium for small Reynolds (*Re*) and viscous Richardson (*Ri_v*) numbers, with $\boldsymbol{u}'^{(1)}$ corresponding to the lab reference frame with a quiescent far-field ambient (the prime indicates that the velocity field has a disturbance-like character in this reference frame, and decays away in the far-field). The Reynolds and viscous Richardson numbers measure the relative importance of inertial and buoyancy forces relative to viscous forces, respectively, and the aforementioned smallness of these parameters corresponds therefore to the case where inertia and stratification act as weak perturbing influences about a leading-order Stokesian approximation; note, however, that the result for the stratification torque obtained in § 4.1 is an exception to this general assumption, in that it continues to be valid for finite values of the Richardson number. The Reynolds and Richardson numbers are defined later in this section when writing down the non-dimensional system of governing equations; the precise definition of the dynamic stress field, $\boldsymbol{\sigma}^{(1d)}$, is also provided at the same place.

The pair $(\boldsymbol{\sigma}^{(2)}, \boldsymbol{u}^{(2)})$, that defines the test problem in (2.1), corresponds to the stress and velocity fields associated with inertialess $(Re = 0)$ rotation of the same spheroid, about an axis orthogonal to its axis of symmetry, in a homogeneous and otherwise quiescent ambient with the same (assumed constant) viscosity as the medium in the actual problem. The equations governing the test problem may be written as

$$\frac{\partial u_i^{(2)}}{\partial x_i} = 0, \qquad (2.2)$$

$$\mu \frac{\partial^2 u_i^{(2)}}{\partial x_j^2} - \frac{\partial p^{(2)}}{\partial x_i} = 0, \qquad (2.3)$$

with the boundary condition $\boldsymbol{u}^{(2)} = \boldsymbol{\Omega}^{(2)} \wedge \boldsymbol{x}$ on S_p, $\boldsymbol{\Omega}^{(2)}$ being the angular velocity of the spheroid in the test problem, and far-field decay conditions for both $\boldsymbol{u}^{(2)}$ and $p^{(2)}$.

933 A17-4

Note that the test velocity ($u^{(2)}$) and stress ($\sigma^{(2)}$) fields decay as $O(1/r^2)$ and $O(1/r^3)$, respectively, r being the distance away from the spheroid; this decay, together with the decaying (dynamic) stress field in the problem of interest, justifies the neglect of the surface integrals at infinity in (2.1). Use of the aforementioned surface boundary condition in (2.1) leads to

$$\int_{S_p} \sigma_{ij}^{(2)} u_i'^{(1)} n_j \, \mathrm{d}S - \Omega_j^{(2)} \int_{S_p} \epsilon_{ijk} x_k \sigma_{il}^{(1d)} n_l \, \mathrm{d}S = \int \frac{\partial \sigma_{ij}^{(1d)}}{\partial x_j} u_i^{(2)} \, \mathrm{d}V, \qquad (2.4)$$

where the second integral on the left-hand side in (2.4) now denotes the torque due to the dynamic stress field $\sigma^{(1d)}$. We postpone further simplification of (2.4) until after we define the pair ($\sigma^{(1d)}$, $u'^{(1)}$).

As mentioned previously, problem 1 corresponds to an arbitrarily oriented spheroid, sedimenting under the action of a gravitational force $F\hat{g}$, in an ambient fluid that is linearly stratified (along $\hat{g}$) in the absence of the fluid motion induced by the spheroid. The unit vector $\hat{g}$ is aligned along gravity, with g denoting the magnitude of the gravitational acceleration, and $F = (4\pi/3)Lb^2 \Delta\rho g((4\pi/3)L^2 b\Delta\rho g)$ denoting the buoyant weight for a prolate (oblate) spheroid. Here, L and b are the semi-major and semi-minor axes of the spheroid, with $\kappa = L/b$ and b/L being the aspect ratios of prolate and oblate spheroids, respectively; thus, $\kappa > 1$ and $\kappa < 1$ for the prolate and oblate cases. The density difference that enters the buoyant weight above is $\Delta\rho = \rho_s - \rho_\infty^{(1)}(x_c)$, with ρ_s being the density of the spheroid (assumed homogeneous), and $\rho_\infty^{(1)}(x_c) = \rho_0$ being the ambient fluid density at the centre of the spheroid. The latter simplification arises because of the linear stratification and the fore–aft symmetry of the spheroid, both of which imply that the weight of the equivalent stratified spheroidal fluid blob that gives the buoyant force, within an Archimedean interpretation, is the same as the weight of a homogeneous fluid blob with density equal to the ambient value at the spheroid centre. In a lab-fixed reference frame, the ambient density field in problem 1 may be written in the form:

$$\rho_\infty^{(1)}(x^L) = \rho_0 + \gamma x_i^L \hat{g}_i, \qquad (2.5)$$

where x^L denotes the position vector in laboratory coordinates with the spheroid centre as the origin, and $\gamma > 0$ is the constant density gradient that characterizes the stable ambient stratification. The calculations for the torque are, however, best done in a reference frame translating with the spheroid where a quasi-steady state is assumed to prevail at leading order. The latter assumption is motivated by the asymptotically weak rotation of the sedimenting spheroid in the limit $Re, Ri_v \ll 1$. The precise condition for the quasi-steady state assumption to hold depends on Pe, being more restrictive for large Pe, and is stated later alongside the results for the spheroid angular velocity for small and large Pe, obtained in the following.

The ambient density in the particle-fixed reference frame takes the form:

$$\rho_\infty^{(1)}(x) = \rho_0 + \gamma (x_i + U_i t)\hat{g}_i, \qquad (2.6)$$

x being the position vector in the new reference frame. In (2.6), U is the spheroid settling velocity, and related to the force ($F\hat{g}$) via a mobility tensor that is a known function of the spheroid aspect ratio κ. In terms of the spheroid orientation vector p, one may write $U = (1/\mu L)[X_A^{-1} pp + Y_A^{-1}(I - pp)] \cdot (F\hat{g})$, $X_A(\kappa)$ and $Y_A(\kappa)$ being the non-dimensional axial and transverse translational resistance functions. The aspect ratio dependence of these functions is well known (see Kim & Karrila 1991), and is given in Appendix A for

convenient reference. Note that the ambient density at the centre of the spheroid ($x = 0$) is given by $\rho_0 + \gamma(U_i\hat{g}_i)t$, the time dependence arising from the spheroid translation. The equations of motion for problem 1, within a Boussinesq framework where the fluid density multiplying the inertial terms is taken as a constant ρ_0 (say), may be written as

$$\frac{\partial u_i^{(1)}}{\partial x_i} = 0, \tag{2.7}$$

$$\mu\frac{\partial^2 u_i^{(1)}}{\partial x_j^2} - \frac{\partial p^{(1)}}{\partial x_i} = \rho_0 u_j^{(1)}\frac{\partial u_i^{(1)}}{\partial x_j} - \rho^{(1)}g_i, \tag{2.8}$$

$$\frac{\partial \rho^{(1)}}{\partial t} + u_j^{(1)}\frac{\partial \rho^{(1)}}{\partial x_j} = D\nabla^2\rho^{(1)}, \tag{2.9}$$

where D is the diffusivity of the stratifying agent (Candelier, Mehaddi & Vauquelin 2014; Mehaddi *et al.* 2018; Shaik & Ardekani 2020). One now defines the perturbation density ($\rho'^{(1)}$) via $\rho^{(1)} = \rho_0 + \gamma(x_i + U_it)\hat{g}_i + \rho'^{(1)}$. Next, using the scales $U = F/(\mu L X_A)$ for the velocity, L for the length, $\mu U/L$ for the pressure and γL for $\rho'^{(1)}$, one obtains the following system of non-dimensional equations:

$$\frac{\partial u_i^{(1)}}{\partial x_i} = 0, \tag{2.10}$$

$$\frac{\partial^2 u_i^{(1)}}{\partial x_j^2} - \frac{\partial p^{(1)}}{\partial x_i} + \frac{\rho_0 g L^2}{\mu U}\hat{g}_i + Ri_v(\hat{U}_jt + x_j)\hat{g}_j\hat{g}_i = Re\, u_j^{(1)}\frac{\partial u_i^{(1)}}{\partial x_j} - Ri_v\rho'^{(1)}\hat{g}_i, \tag{2.11}$$

$$u_j^{(1)}\frac{\partial \rho'^{(1)}}{\partial x_j} + (\hat{U}_j + u_j^{(1)})\hat{g}_j = \frac{1}{Pe}\nabla^2\rho'^{(1)}, \tag{2.12}$$

where $Re = \rho_0 UL/\mu$, $Ri_v = \gamma L^3 g/(\mu U)$ and $Pe = UL/D$ are the Reynolds, viscous Richardson and Péclet numbers, respectively; note that $Ri_v = Re/Fr^2$, where Fr is the Froude number, and the usual measure of the importance of stratification in the inviscid limit (Turner 1973). In (2.10)–(2.12), we continue to use the same notation for the dimensionless fields for simplicity. The velocity fields, in the lab reference frame used in (2.1), and in the particle-fixed reference frame adopted in (2.10)–(2.12) are related as $\boldsymbol{u}'^{(1)} = (\hat{U} + \boldsymbol{u}^{(1)})$, with $\hat{U} = [p_ip_j + X_A/Y_A(\delta_{ij} - p_ip_j)]\hat{g}_j$, now being a dimensionless vector along the direction of settling, and $-\hat{U}$ therefore being the far-field ambient flow in the particle-fixed frame; note that $\hat{U}$ is not a unit vector for an arbitrarily oriented spheroid, and reduces to one only for a spheroid aligned with gravity. Thus, the combination $(\hat{U} + \boldsymbol{u}^{(1)})\cdot\hat{\boldsymbol{g}}$ in (2.12) denotes the convection of the (constant) base-state density gradient by the component of the disturbance velocity field ($u'^{(1)}_3$) along gravity. Finally, the time dependence of $\boldsymbol{u}^{(1)}$ in (2.11), and that of $\rho'^{(1)}$ in (2.12) in particular, that arise from the (slow) rotation of the spheroid, have been neglected owing to the quasi-steady state assumption made in (2.10)–(2.12); the time dependence of the density multiplying the inertial terms, on account of spheroid translation, has already been neglected within the Boussinesq approximation.

One now defines a disturbance pressure field ($p'^{(1)}$) via $p^{(1)} = p_0^{(1)} + p'^{(1)}$ with

$$\frac{\partial p_0^{(1)}}{\partial x_i} = \frac{\rho_0 g L^2}{\mu U}\hat{g}_i + Ri_v(\hat{U}_jt + x_j)\hat{g}_j\hat{g}_i, \tag{2.13}$$

so that $p_0^{(1)}$ defines the baseline hydrostatic contribution arising from the ambient linear stratification. Having incorporated the baseline hydrostatic variation in $p_0^{(1)}$, one may write the governing equations above in terms of the disturbance velocity, pressure and density fields as follows:

$$\frac{\partial u_i'^{(1)}}{\partial x_i} = 0, \tag{2.14}$$

$$\frac{\partial \sigma_{ij}^{(1d)}}{\partial x_j} = Re(-\hat{U}_j + u_j'^{(1)}) \frac{\partial u_i'^{(1)}}{\partial x_j} - Ri_v \rho'^{(1)} \hat{g}_i, \tag{2.15}$$

$$(-\hat{U}_j + u_j'^{(1)}) \frac{\partial \rho'^{(1)}}{\partial x_j} = -u_j'^{(1)} \hat{g}_j + \frac{1}{Pe} \nabla^2 \rho'^{(1)}. \tag{2.16}$$

where the left-hand side of (2.11) has been written in terms of the dynamic stress field $\boldsymbol{\sigma}^{(1d)}$ defined by $\boldsymbol{\sigma}^{(1d)} = -p'^{(1)} \boldsymbol{I} + (\nabla \boldsymbol{u}'^{(1)} + \nabla \boldsymbol{u}'^{(1)\dagger})$. Thus, one has the relation $\boldsymbol{\sigma}^{(1)} = -p_0^{(1)} \boldsymbol{I} + \boldsymbol{\sigma}^{(1d)}$ between the total ($\boldsymbol{\sigma}^{(1)}$) and the dynamic stress fields of problem 1.

Assuming the spheroid in problem 1 to rotate with an angular velocity $\boldsymbol{\Omega}^{(1)}$, one has the boundary condition $\boldsymbol{u}'^{(1)} = \boldsymbol{\Omega}^{(1)} \wedge \boldsymbol{x}$ on S_p. Using this in the first surface integral in (2.4), and substituting the divergence of the dynamic stress from (2.15) in the volume integral in (2.1), one obtains

$$\Omega_j^{(1)} \mathcal{L}_j^{(2)} - \Omega_j^{(2)} \mathcal{L}_j^{\sigma(1)d} = Re \int u_i^{(2)} (-\hat{U}_j + u_j'^{(1)}) \frac{\partial u_i'^{(1)}}{\partial x_j} \, dV - Ri_v \int \rho'^{(1)} \hat{g}_i u_i^{(2)} \, dV, \tag{2.17}$$

where $\mathcal{L}^{\sigma(1)d}$ now denotes the torque contribution due to the dynamic stress $\boldsymbol{\sigma}^{(1d)}$. Now, the particle in problem 1 is torque-free. In light of the above relation between $\boldsymbol{\sigma}^{(1)}$ and $\boldsymbol{\sigma}^{(1d)}$, the total torque ($\mathcal{L}^{(1)}$) may be written as $\mathcal{L}^{(1)} = \mathcal{L}^{\sigma(1)d} + \mathcal{L}^{\sigma(1)s}$, where the dynamic torque component $\mathcal{L}^{\sigma(1)d}$ includes both inertia and stratification-induced contributions, whereas $\mathcal{L}^{\sigma(1)s}$ is the hydrostatic contribution owing to the pressure field $p_0^{(1)}$ associated with the linearly varying density field of the stably stratified ambient, and defined by (2.13). Thus, $\mathcal{L}^{(1)} = 0 \Rightarrow \mathcal{L}^{\sigma(1)d} = -\mathcal{L}^{\sigma(1)s}$, and the relation involving the spheroid angular velocity in problem 1 takes the following form:

$$\Omega_j^{(1)} \mathcal{L}_j^{(2)} = Re \int u_i^{(2)}(-\hat{U}_j + u_j'^{(1)}) \frac{\partial u_i'^{(1)}}{\partial x_j} \, dV - \left[\Omega_j^{(2)} \mathcal{L}_j^{\sigma(1)s} + Ri_v \int \rho'^{(1)} \hat{g}_i u_i^{(2)} \, dV \right], \tag{2.18}$$

where

$$\mathcal{L}_i^{\sigma(1)s} = -\epsilon_{ijk} \int_{S_p} p_0^{(1)} x_j n_k \, dS, \tag{2.19}$$

with $p_0^{(1)}$ being defined in (2.13). As the buoyancy force in a homogeneous ambient acts through the centre of the spheroid, only the linearly varying term in (2.13) contributes to

933 A17-7

the hydrostatic torque, which may therefore be written as

$$\mathcal{L}_i^{\sigma(1)s} = -Ri_v \, \epsilon_{ijk} \int_{S_p} \frac{1}{2} (x_l \hat{g}_l)^2 x_j n_k \, \mathrm{d}S, \tag{2.20}$$

the contribution above remaining the same regardless of the choice of reference frame (x or x^L). On substitution of the above expression for $\mathcal{L}_k^{\sigma(1)s}$, and using the relation $u_i^{(2)} = U_{ij}^{(2)} \Omega_j^{(2)}$ (on account of the linearity of the Stokes equations), the second-order tensor $U_{ij}^{(2)}$ being known in closed form (see Dabade *et al.* 2015, and § 3), (2.18) takes the form

$$\Omega_j^{(1)} \mathcal{L}_j^{(2)} = \Omega_k^{(2)} \left\{ Re \int U_{jk}^{(2)} (-\hat{U}_l + u_l'^{(1)}) \frac{\partial u_j'^{(1)}}{\partial x_l} \, \mathrm{d}V \right.$$

$$\left. -Ri_v \left[-\frac{1}{2} \epsilon_{klm} \int_{S_p} (x_j \hat{g}_j)^2 x_l n_m \, \mathrm{d}S + \int \rho'^{(1)} \hat{g}_j \, U_{jk}^{(2)} \, \mathrm{d}V \right] \right\}, \tag{2.21}$$

Again, on account of linearity, one may write the torque on the rotating spheroid in the test problem, in the form $\mathcal{L}^{(2)} = [X_C pp + Y_C (I - pp)] \cdot \Omega^{(2)}$, where $X_C(\kappa)$ and $Y_C(\kappa)$ are the non-dimensional axial and transverse rotational resistance functions, and are known functions of κ (Kim & Karrila 1991) whose expressions are given in Appendix A. By symmetry, the sedimenting spheroid cannot spin about its axis regardless of its orientation, and therefore without loss of generality, the test problem can be taken as that of a transverse rotation in the inertialess limit ($\Omega^{(2)} \cdot p = 0$), in which case the test torque–angular velocity relation takes the simpler form $\mathcal{L}^{(2)} = Y_C \Omega^{(2)}$. Finally, accounting for the fact that the test angular velocity $\Omega^{(2)}$ can point in an arbitrary direction in a plane perpendicular to p, one obtains the following relation for the spheroid angular velocity in problem 1:

$$\Omega_i^{(1)} = \frac{1}{Y_C} \left\{ Re \int U_{ji}^{(2)} (-\hat{U}_l + u_l'^{(1)}) \frac{\partial u_j'^{(1)}}{\partial x_l} \, \mathrm{d}V + Ri_v \left[\epsilon_{ilm} \int_{S_p} \frac{1}{2} (x_j \hat{g}_j)^2 x_l n_m \, \mathrm{d}S \right. \right.$$

$$\left. \left. - \int \rho'^{(1)} \hat{g}_j \, U_{ji}^{(2)} \, \mathrm{d}V \right] \right\}. \tag{2.22}$$

As a settling spheroid in a homogeneous ambient must retain its initial orientation in the Stokes limit on account of reversibility, expectedly, the rotation of the spheroid, as given by (2.22), arises due to the combined (weak) effects of fluid inertia and the ambient stratification. The first term within the curly brackets in (2.22) corresponds to the inertial torque, whereas the second and third terms which have been grouped together (within square brackets) correspond to the hydrostatic and hydrodynamic components of the stratification torque, respectively. The hydrostatic torque only involves knowledge of the ambient density field, and is easily evaluated. The inertial torque has a regular character in that the dominant contributions to the $O(Re)$ volume integral in (2.22) arise from a volume of $O(L^3)$ around the sedimenting spheroid, and therefore, the integral may again readily be determined at leading order using Stokesian approximations for the velocity fields involved, as has been done in Dabade *et al.* (2015). The evaluation of these two simpler contributions is detailed in the next section. The nature of the hydrodynamic torque arising from the perturbed stratification depends crucially on *Pe*, and this more complicated calculation is given in §§ 4.1 and 4.2, for small and large *Pe*, respectively.

3. The spheroidal angular velocity due to the inertial and hydrostatic torque contributions

The $O(Re)$ inertial angular velocity in (2.22) has recently been calculated for spheroids, both prolate and oblate, of an arbitrary aspect ratio (see Dabade *et al.* 2015). Although the analysis in Dabade *et al.* (2015) pertains to the limit $Re \ll 1$, the results have been shown to remain qualitatively valid even for Re of order unity (see Jiang *et al.* 2020). As mentioned previously, this angular velocity has a regular character, as may be seen from the convergence of the inertial volume integral in (2.18) based on the leading-order Stokesian estimate for the integrand. As argued in Dabade *et al.* (2015), the inertial acceleration $\boldsymbol{u}^{(1)} \cdot \nabla \boldsymbol{u}'^{(1)} \sim \hat{U} \cdot \nabla \boldsymbol{u}'^{(1)} \sim O(1/r^2)$ for distances large compared with L, or $r \gg 1$ in dimensionless terms, on using $\boldsymbol{u}'^{(1)} \sim O(1/r)$ for the Stokeslet field due to the translating spheroid. The test velocity field $\boldsymbol{u}^{(2)}$ due to the rotating spheroid has the character of a rotlet-cum-stresslet in the far-field, and is therefore $O(1/r^2)$. This leads to an integrand that decays as $\hat{U} \cdot \nabla \boldsymbol{u}'^{(1)} \cdot \boldsymbol{u}^{(2)} \sim O(1/r^4)$ for $r \gg 1$, implying a convergent volume integral. This volume integral has been evaluated in closed form using spheroidal coordinates in Dabade *et al.* (2015). For the prolate case, the spheroidal coordinates (ξ, η, ϕ) are defined by the relations: $x_1 + ix_2 = d\bar{\xi}\bar{\eta} \exp(i\phi)$, $x_3 = d\xi\eta$, with the three axes of the Cartesian system ($\boldsymbol{1}_3$) aligned with the spheroid axis of symmetry. Here, $1 \le \xi < \infty$, $|\eta| \le 1$ and $0 \le \phi < 2\pi$, with $\bar{\xi} = (\xi^2 - 1)^{1/2}$ and $\bar{\eta} = (1 - \eta^2)^{1/2}$. The constant-$\xi$ surfaces correspond to confocal prolate spheroids and the constant-η surfaces to confocal two-sheeted hyperboloids, both with the interfoci distance $2d$, and the constant-ϕ surfaces are planes passing through the axis of symmetry. The corresponding expressions for the oblate case may be obtained by the substitutions $d \leftrightarrow -id$, $\xi \leftrightarrow i\bar{\xi}$, the constant-$\xi$ and η surfaces now being confocal oblate spheroids and single-sheeted hyperboloids, respectively. In either case, the spheroid is the surface $\xi = \xi_0$, its aspect ratio being given by $\kappa = \xi_0/\bar{\xi}_0$ and $\bar{\xi}_0/\xi_0$ for prolate and oblate spheroids; thus, the near-spherical limit ($\kappa \to 1$) for either prolate or oblate spheroids corresponds to $\xi_0 \to \infty$, whereas the slender fiber ($\kappa \to \infty$) and flat disk ($\kappa \to 0$) limits correspond to $\xi_0 \to 1$. The fluid domain in the volume integrals in (2.22) corresponds to $\xi \ge \xi_0$.

For a prolate spheroid, the actual velocity field $\boldsymbol{u}'^{(1)}$ and the test velocity field tensor $\boldsymbol{U}^{(2)}$ in (2.22), may be written in the form (see Dabade *et al.* 2015, 2016):

$$\boldsymbol{u}'^{(1)} = \left(\frac{\hat{U} \cdot \boldsymbol{1}_3}{\xi_0 Q_1^1(\xi_0) + Q_0^0(\xi_0)} \right) \boldsymbol{S}_{1,0}^{(3)} + \left(\frac{\hat{U} \cdot \boldsymbol{1}_1}{3Q_0^0(\xi_0) - \xi_0 Q_1^1(\xi_0)} \right) (\boldsymbol{S}_{1,1}^{(3)} - \boldsymbol{S}_{1,-1}^{(3)}), \quad (3.1)$$

$$\boldsymbol{U}^{(2)} = \boldsymbol{1}_2 \left(\frac{d(2\xi_0^2 - 1)(\boldsymbol{S}_{1,1}^{(2)} - \boldsymbol{S}_{1,-1}^{(2)})}{\left[2\xi_0 Q_1^0(\xi_0) - \sqrt{\xi_0^2 - 1} Q_1^1(\xi_0) \right]} + \frac{d \left[\xi_0 Q_1^1(\xi_0) + 2\sqrt{\xi_0^2 - 1} Q_1^0(\xi_0) \right] (\boldsymbol{S}_{2,1}^{(3)} - \boldsymbol{S}_{2,-1}^{(3)})}{Q_2^1(\xi_0) \left[2\xi_0 Q_1^0(\xi_0) - \sqrt{\xi_0^2 - 1} Q_1^1(\xi_0) \right]} \right). \quad (3.2)$$

The $\boldsymbol{S}_{t,s}^{(3)}$ and $\boldsymbol{S}_{t,s}^{(2)}$ in (3.1) and (3.2) denote the decaying (biharmonic and harmonic) vectorial solutions of the Stokes equations in spheroidal coordinates, and are given in Appendix C; the $Q_t^s(\xi)$ denote the associated Legendre functions of the second kind. Using these expressions, the volume integration may then be carried out analytically, and the inertial angular velocity ($\boldsymbol{\Omega}^{(1)I}$) is given by

$$\Omega_i^{(1)I} = Re \left[\frac{F_I^p(\xi_0) X_A}{Y_C Y_A} (\epsilon_{ijk} \hat{g}_j p_k \, \hat{g}_l p_l) \right], \quad (3.3)$$
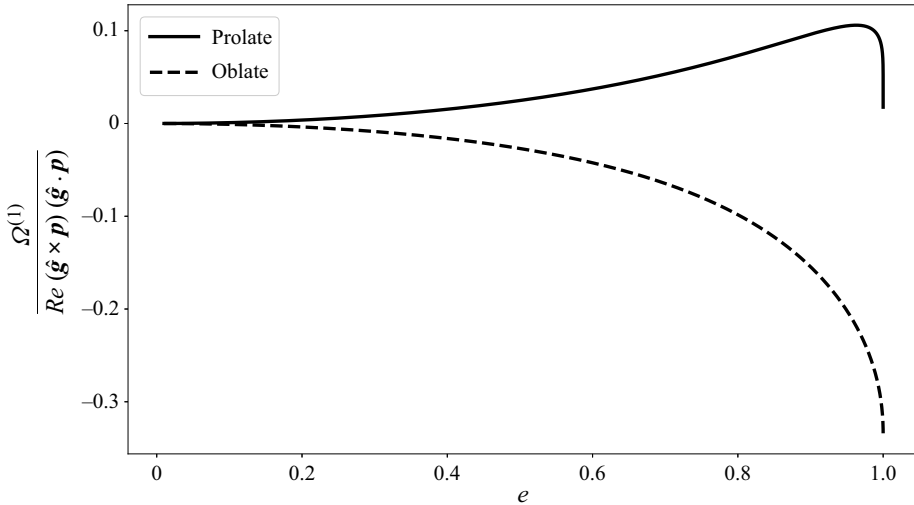
Figure 1. The functions $(F_I^p(\xi_0)X_A)/(Y_C Y_A)$ and $(F_I^o(\xi_0)X_A)/(Y_C Y_A)$, that characterize the aspect ratio dependence of the inertial contributions to the angular velocities of prolate and oblate spheroids in (3.3) and (3.4), plotted as a function of the spheroid eccentricity.

for prolate spheroids. The corresponding expression for the oblate case may be obtained by the aforementioned substitutions, namely $d \leftrightarrow -id$, $\xi_0 \leftrightarrow i\bar{\xi}_0$ in the dimensional angular velocity, and is given by

$$\Omega_i^{(1)I} = Re\left[\frac{F_I^o(\xi_0)X_A}{Y_C Y_A}(\epsilon_{ijk}\hat{g}_j p_k \hat{g}_l p_l)\right]. \tag{3.4}$$

The expressions for $F_I^p(\xi_0)$ and $F_I^o(\xi_0)$, as functions of the spheroid eccentricity ($e = 1/\xi_0$), were first obtained by Dabade *et al.* (2015), and are given in Appendix A. The inertial angular velocity given by (3.3) and (3.4) orients sedimenting spheroids broadside-on regardless of κ. The combination of the aspect-ratio-dependent functions, $F_I^{p/o}(\xi_0)X_A/(Y_C Y_A)$, that multiplies $Re(\hat{g} \cdot p)(\hat{g} \wedge p)$, and that determines the κ-dependence of the inertial angular velocities above, is plotted as a function of the eccentricity in figure 1, for both the prolate and oblate cases. One obtains the expected $O(1/\xi_0^2)$ scaling in the near-sphere limit ($\xi_0 \to \infty$); at the other extreme($\xi_0 \to 1$), the inertial angular velocity approaches zero as $O[\ln(\xi_0 - 1)]^{-1}$ in the slender fiber limit, consistent with viscous slender body theory (Khayat & Cox 1989; Subramanian & Koch 2005), while remaining finite in the limit of a flat disk.

The hydrostatic component of the stratification torque is also readily evaluated in spheroidal coordinates. For the prolate case, the dimensionless position vector that appears in (2.20) is given by $x = (\bar{\xi}_0/\xi_0)\bar{\eta}(\cos\phi\mathbf{1}_1 + \sin\phi\mathbf{1}_2) + \eta\mathbf{1}_3$, and the unit normal is

$$\mathbf{n} = \mathbf{1}_\xi = \frac{\xi_0\bar{\eta}}{\sqrt{\xi_0^2 - \eta^2}}(\cos\phi\mathbf{1}_1 + \sin\phi\mathbf{1}_2) + \frac{\overline{\xi_0}\eta}{\sqrt{\xi_0^2 - \eta^2}}\mathbf{1}_3. \tag{3.5}$$

Using these expressions, and the areal element $dS = h_\eta h_\phi \, d\eta \, d\phi$, with $h_\eta = \sqrt{\xi_0^2 - \eta^2}/\xi_0\bar{\eta}$ and $h_\phi = \bar{\xi}_0\bar{\eta}/\xi_0$, one obtains the angular velocity due to the hydrostatic
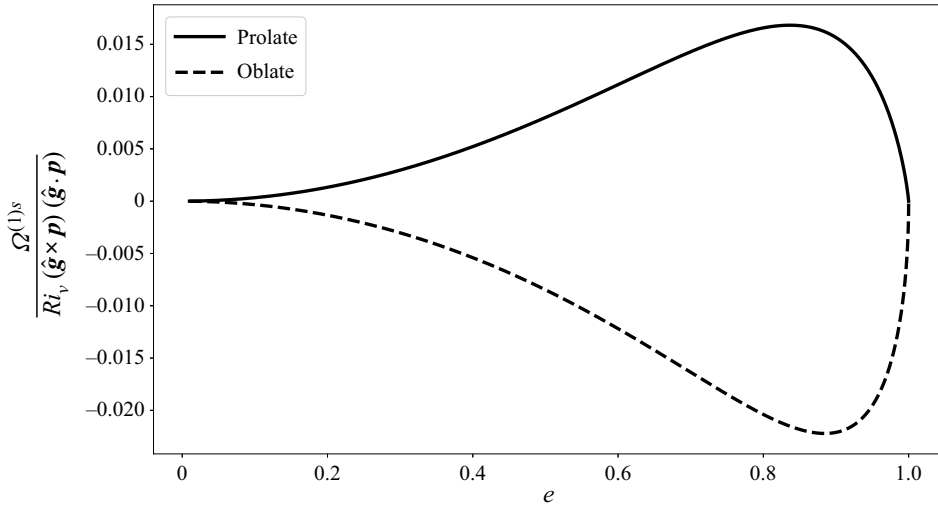
933 A17-10

Figure 2. The aspect-ratio-dependent functions multiplying $Ri_v(\hat{g} \cdot p)(\hat{g} \wedge p)$ in (3.6) and (3.7), that characterize the hydrostatic contributions for prolate and oblate spheroids, plotted as a function of the spheroid eccentricity.

torque as

$$\Omega_i^{(1)s} = Ri_v \frac{4\pi}{15Y_C} \frac{1 - \xi_0^2}{\xi_0^4} (\epsilon_{ijk}\hat{g}_j p_k)(\hat{g}_l p_l), \tag{3.6}$$

for the prolate case, and using the transformations mentioned previously,

$$\Omega_i^{(1)s} = Ri_v \frac{4\pi}{15Y_C} \frac{\sqrt{\xi_0^2 - 1}}{\xi_0^3} (\epsilon_{ijk}\hat{g}_j p_k)(\hat{g}_l p_l), \tag{3.7}$$

for the oblate case. The angular velocities given by (3.6) and (3.7) also orient the spheroid broadside-on like the inertial torque above. The aspect-ratio-dependent functions that multiply $Ri_v(\hat{g} \cdot p)(\hat{g} \wedge p)$ in (3.6) and (3.7) are plotted as functions of ξ_0 in figure 2. As the hydrostatic torque is only a function of the particle geometry, these aspect ratio functions are algebraically small in both the near-sphere, and the slender fiber and flat-disk limits.

The inertial and hydrostatic angular velocities above have an identical angular dependence, of the form $(\hat{g} \cdot p)(\hat{g} \wedge p)$, one which is easily inferred based on the requirement that the angular velocity be a pseudovector quadratic in $\hat{g}$ (Dabade *et al.* 2015). The dependence implies that the maximum angular velocity occurs midway between the horizontal ($\hat{g} \cdot p = 0$) and vertical ($\hat{g} \cdot p = 1$) orientations. The hydrostatic torque arises because the point of action of the upward buoyant force, the centre of mass of the equivalent stratified fluid blob (in the Archimedean interpretation) lies below the geometric centre through which the weight of the spheroid acts vertically downward. The two forces therefore constitute a couple that turns the spheroid broadside-on. The broadside-on nature of the inertial torque is on account of 'wake-shielding': the wake associated with the front portion of the spheroid shields the rear, which catches up with the front as a result. As pointed out in Dabade *et al.* (2015), this is not literally true for small *Re*. A signature of the wake arises only on length scales greater than $O(LRe^{-1})$, the Oseen region, in contrast to the scaling arguments above which show that the $O(Re)$

inertial torque arises from fluid inertial forces in a region of $O(L^3)$ (the inner region) around the sedimenting spheroid. Nevertheless, the velocity field in the inner region reflects the asymmetry of the outer Oseen field, and the sense of rotation remains the same for small Re. Importantly, the broadside-on nature of the inertial and hydrostatic torques imply that the transition from broadside-on to edgewise settling, observed in the recent experiments (see Mercier *et al.* 2020) discussed in the introduction, must depend entirely on the hydrodynamic component of the stratification torque, that is, the second term within square brackets on the right-hand side in (2.22). While the calculation above shows the hydrostatic component to be $O(Ri_v)$, consistent with the nominal order in (2.22), this is not true of the hydrodynamic component. As shown in § 4, the hydrodynamic component scales as $O(Ri_v)$ only for sufficiently small $Pe(\ll Ri_v^{3/5}$ for $Ri_v \ll 1$; see § 4.1.1), when the dominant contribution to the associated torque integral comes from length scales of $O(L)$ similar to the inertial torque above. In the opposite limit, and for the so-called Stokes stratification regime corresponding to $Re \ll Ri_v^{1/3}$ (see Mehaddi *et al.* 2018; Varanasi & Subramanian 2021), the dominant contributions to the torque integral arise from much larger length scales of $O(LRi_v^{-1/3})$, and the hydrodynamic component scales as $O(Ri_v^{2/3})$, being much larger than the hydrostatic component above.

Before proceeding with the calculation of the hydrodynamic component of the stratification torque, it is worth remarking on the nature of the coupling between the inertial and stratification torque contributions that is not obvious from the formal result (2.22), where they appear as separate additive contributions. On account of the convergent volume integral, the $O(Re)$ inertial angular velocity, as given by (3.3) and (3.4), only involves the Stokesian fields in a homogeneous ambient, and is evidently independent of the ambient stratification. The correction to this leading-order estimate is dependent on the nature of the ambient stratification, however, even within the Boussinesq framework. To see this, we return to the inertial volume integral, and estimate the next correction. Recall that the angular velocities in (3.3) and (3.4) were based on the approximating the volume integral by Stokesian estimates, and the torque contribution at the next order requires one to examine the next term in the small-Re expansion for the velocity field in problem 1. Writing $\boldsymbol{u}'^{(1)} = \boldsymbol{u}'^{(10)} + Re\,\boldsymbol{u}'^{(11)}$, $\boldsymbol{u}'^{(10)}$ is the Stokesian approximation given by (3.1) and is $O(1/r)$ for $r \gg 1$, whereas $\boldsymbol{u}'^{(11)}$ remains $O(1)$ in the far-field. The latter, of course, implies that the above regular expansion breaks down at length scales of $O(LRe^{-1})$, a manifestation of the singular nature of inertia in an unbounded domain (the so-called Whitehead's paradox; see Leal 1992). Provided one assumes buoyancy forces to dominate the inertial ones on scales much smaller than the inertial screening length (of $O(LRe^{-1})$), the above far-field estimate of $\boldsymbol{u}'^{(11)}$ may still be used to estimate the correction to the leading $O(Re)$ contribution. The $O(Re^2)$ inertial acceleration is now $\hat{\boldsymbol{U}} \cdot \boldsymbol{\nabla} \boldsymbol{u}'^{(11)} \sim O(1/r)$, and using $\boldsymbol{u}^{(2)} \sim O(1/r^2)$, the resulting volume integral, at $O(Re^2)$, is logarithmically divergent. The divergence will be cut off at the stratification screening length that is $O(Ri_v Pe)^{-1/4}$ for $Pe \ll 1$ (List 1971; Ardekani & Stocker 2010), and $O(Ri_v^{-1/3})$ for $Pe \gg 1$ (Mehaddi *et al.* 2018; Varanasi & Subramanian 2021), implying that the next correction to the inertial angular velocity is $O[Re^2 \ln(Ri_v Pe)^{-1/4}]$ for $Pe \ll 1$ and $O(Re^2 \ln Ri_v^{-1/3})$ for $Pe \gg 1$, and is thereby a function of the ambient stratification. For self consistency, one requires that both of the aforementioned stratification screening lengths be less than $O(Re^{-1})$, which translates to the requirement $Ri_v \gg Pe^{-1}Re^4$ for small Pe, and for one to be in the aforementioned Stokes stratification regime ($Ri_v^{1/3} \gg Re$) for large Pe.

4. The spheroidal angular velocity due to the hydrodynamic component of the stratification contribution

Owing to the differing character of the hydrodynamic component in the limits of small and large Pe, the calculations in these two asymptotic regimes are carried out in separate subsections here. Keeping in mind that $Pe = RePr$, Pr being the Prandtl number, the small Pe case does not necessarily place a restriction on Pr which may either be small or large (although, large Pr imposes a greater restriction on the smallness of Re because Re must now be smaller than $O(Pr^{-1})$). However, the assumption of small Re implies that the large Pe case necessarily requires a large Pr which may be realized in experiments that use salt as a stratifying agent.

4.1. *The hydrodynamic stratification torque in the diffusion-dominant limit* ($Pe \ll 1$)

In the limit $Pe \ll 1$, one may neglect the convective terms in the advection diffusion equation (2.16), and the density perturbation $\rho'^{(1)}$ in the stratification torque integral therefore arises as a diffusive response to the no-flux condition that must be satisfied on the spheroid surface. As a result, the spheroid acts as a concentration-dipole singularity in the far-field ($r \gg 1$), implying that $\rho'^{(1)}$ must decay as $O(1/r^2)$. As the test velocity field $u^{(2)}$ corresponding to the rotating spheroid also decays as $O(1/r^2)$, the integrand is $O(1/r^4)$ for $r \gg 1$. This decay is the same as that of the inertial integrand estimated above, and the integral for the hydrodynamic stratification torque is therefore convergent for small Pe, based on the leading-order diffusive estimates above. Thus, the effects of stratification arise as a regular perturbation for small Pe, or said differently, the dominant contribution to the hydrodynamic component of the stratification torque arises from buoyancy forces in a volume of $O(L^3)$ around the sedimenting spheroid. As a consequence and as is shown in the following, for small Pe, the hydrodynamic component is $O(Ri_v)$ similar to the hydrostatic component given in (3.6) and (3.7). It turns out that there is, in fact, a more severe constraint on the Péclet number; as explained in § 4.1.1, the $O(Ri_v)$ scaling for the hydrodynamic component holds only when $Pe \ll Ri_v^{3/5} \ll 1$.

To determine the detailed dependence of the $O(Ri_v)$ hydrodynamic component on κ, one needs to solve for the density perturbation $\rho'^{(1)}$ which satisfies

$$\nabla^2 \rho'^{(1)} = 0 \tag{4.1}$$

in the fluid domain $\xi \geq \xi_0$. The no-flux boundary condition on the spheroid surface ($\xi = \xi_0$) may be written as $\mathbf{1}_\xi \cdot \nabla \rho'^{(1)} = -\mathbf{1}_\xi \cdot \hat{\mathbf{g}}$ where we have used that $\mathbf{n} = \mathbf{1}_\xi$, and the right-hand side of the boundary condition arises from the gradient of the linearly varying ambient density; there is the additional requirement of far-field decay, namely $\rho'^{(1)} \to 0$ for $\xi \to \infty$. Note that the linearity of the governing equation (4.1) and the boundary conditions in $\rho'^{(1)}$, and the linear dependence on $\hat{\mathbf{g}}$ of the surface boundary condition above, imply that $\rho'^{(1)}$ must be linear in $\hat{\mathbf{g}}$ at leading order for small Pe. From (2.22), the hydrodynamic component of the stratification torque must therefore be quadratic in $\hat{\mathbf{g}}$. This implies that the hydrodynamic torque must have an angular dependence identical to the inertial and hydrostatic contributions, of the form $(\hat{\mathbf{g}} \wedge \mathbf{p})(\hat{\mathbf{g}} \cdot \mathbf{p})$, with a multiplicative pre-factor that is a function of κ. Thus, for small Pe, the ratio of the hydrostatic and hydrodynamic components of the stratification torque is independent of the spheroid orientation and Ri_v, and only a function of κ.

To solve (4.1), we write down the explicit form of the no-flux boundary condition, in prolate spheroidal coordinates:

$$\frac{\partial \rho'^{(1)}}{\partial \xi}\bigg|_{\xi=\xi_0} = \frac{(P_1^1(\eta)e^{i\phi} - 2P_1^{-1}(\eta)e^{i\phi})}{2\bar{\xi}_0} \sin \psi - \frac{P_1^0(\eta)}{\xi_0} \cos \psi, \tag{4.2}$$

where ψ denotes the angle between $\boldsymbol{p}$ and $\boldsymbol{g}$; in (4.2), and $P_t^s(\xi)$ is the associated Legendre function of the first kind with $P_1^{-1}(\eta) = -P_1^1(\eta) = -(\bar{\eta}/2)$ and $P_1^0(\eta) = \eta$. The η-dependence of the solution is imposed by that of the boundary condition above. This, and the fact that the Laplacian is separable in spheroidal coordinates with the eigenfunctions in ξ and η being the associated Legendre functions of the second and the first kind, respectively, points to the following ansatz for $\rho'^{(1)}$:

$$\rho'^{(1)} = A_{1,1}Q_1^1(\xi)P_1^1(\eta)e^{i\phi} + A_{1,-1}Q_1^{-1}(\xi)P_1^{-1}(\eta)e^{-i\phi} + A_{1,0}Q_1^0(\xi)P_1^0(\eta), \tag{4.3}$$

where $Q_1^{-1}(\xi) = Q_1^1(\xi)/2$, the latter being defined in Appendix C (see (C7)). Substitution of (4.3) leads to the following expressions for the $A_{i,j}$ in (4.3):

$$A_{1,1} = \frac{\bar{\xi}_0^2}{4 - 2\xi_0^2 + 2\xi_0\bar{\xi}_0^2 \coth^{-1}\xi_0} \sin \psi, \tag{4.4}$$

$$A_{1,-1} = -4A_{1,1}, \tag{4.5}$$

$$A_{1,0} = \frac{\bar{\xi}_0^2}{\xi_0(\xi_0 - \bar{\xi}_0^2 \coth^{-1}\xi_0)} \cos \psi. \tag{4.6}$$

The first two terms in (4.3) correspond to the density perturbation induced by a spheroid oriented transversely to gravity, whereas the third term corresponds to that induced by a spheroid aligned with gravity. The expressions for the $A_{i,j}$ above are therefore consistent with the underlying linearity of the problem, in that the perturbation induced by an arbitrarily oriented spheroid is obtained as a superposition of the transverse and longitudinal problems, the factors involved in this superposition being $\sin \psi$ and $\cos \psi$, respectively.

The density perturbation from (4.3), together with (4.4)–(4.6), and the test velocity field from (3.2) are now substituted in the integral for the hydrodynamic stratification torque in (2.22). The volume integration is carried out in the spheroidal coordinate system introduced in § 3, and leads to the following expression for the angular velocity:

$$\Omega_i^{(1)d} = Ri_v \frac{F_s^{p/o}(\xi_0)}{Y_C} (\epsilon_{ijk}\hat{g}_j p_k)(\hat{g}_l p_l), \tag{4.7}$$

with

$$F_s^p(\xi_0) = 2\pi\overline{\xi}_0^2$$

$$\frac{\left((7\xi_0^5 - 7\xi_0^3 - 2\xi_0) + \overline{\xi}_0^2 C_p \left(-12\xi_0^4 + 6\xi_0^2 + \xi_0 C_p \left(3\xi_0^4 + 2\left(\xi_0^5 - \xi_0\right)C_p - 6\xi_0^2 + 7\right) - 2\right)\right)}{15\xi_0^5 \left(\xi_0 - \overline{\xi}_0^2 C_p\right)\left(-\xi_0^2 + \overline{\xi}_0^2 \xi_0 C_p + 2\right)\left((\xi_0^2 + 1)C_p - \xi_0\right)}, \tag{4.8}$$
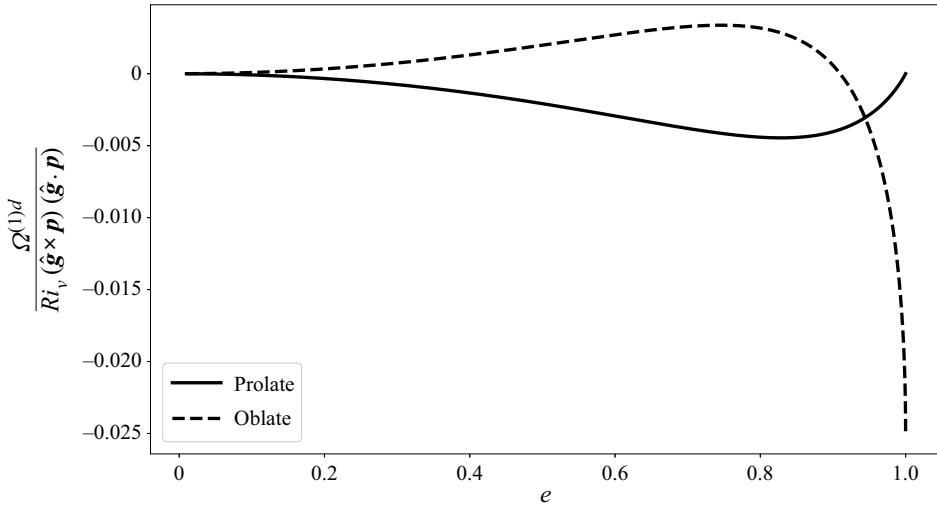
Figure 3. The aspect-ratio-dependent functions, given by (4.8) and (4.9) divided by Y_C, that characterize the hydrodynamic stratification-induced contribution for prolate and oblate spheroids in the small *Pe* limit, plotted as a function of the spheroid eccentricity.

for prolate spheroids, where $C_p = \coth^{-1} \xi_0$. Using the transformation mentioned in § 3, one obtains

$$F_s^o(\xi_0) = 2\pi$$

$$\frac{\left(\left(7\xi_0^4 - 7\xi_0^2 - 2\right) \bar{\xi}_0 + 2 \left(\xi_0^4 - 3\xi_0^2 + 2\right) \xi_0^4 C_o^3 - 2 \left(6\xi_0^4 - 9\xi_0^2 + 4\right) \xi_0^2 C_o + \left(3\xi_0^4 + 4\right) \bar{\xi}_0 \xi_0^2 C_o^2 \right)}{15\xi_0^3 \left(\xi_0^2 C_o\right) - \bar{\xi}_0\right) \left(\left(\xi_0^2 - 2\right) \left(C_o\right) - \bar{\xi}_0\right) \left(-\xi_0^2 + \bar{\xi}_0 \xi_0^2 C_o - 1\right)},$$

(4.9)

for the oblate case, where $C_o = \cot^{-1} \bar{\xi}_0$. Figure 3 shows a plot of the aspect-ratio-dependent functions given by (4.8) and (4.9), divided by Y_C. The hydrodynamic component of the stratification torque given by (4.8) always orients a prolate spheroid edgewise for small *Pe*. Interestingly, figure 3 shows that (4.9) changes sign below a critical aspect ratio $\kappa_c \approx 0.41$ ($e \approx 0.9$) and, therefore, the hydrodynamic component acts to orient oblate spheroids, with aspect ratios lower than the aforementioned threshold, broadside-on.

The hydrodynamic stratification torque arises due to the flow associated with the baroclinic source of vorticity, although the reciprocal theorem formulation used here bypasses the explicit calculation of this flow. The vorticity arises from the tilting of the isopycnals to the vertical (the direction of gravity) due to the requirement that they meet the spheroidal surface in a normal orientation, consistent with a no-flux constraint. A sketch of the deformed isopycnals in the plane $\phi = 0, \pi$, and the resulting sign of the baroclinic vorticity field ($\propto \nabla \rho \wedge \hat{\boldsymbol{g}}$) in different regions of the fluid domain, appears in figure 4, for both prolate and oblate spheroids. The baroclinically induced flow has a dipolar character in the Stokes limit, and the relative sizes of the different flow quadrants are set by the pair of singular isopycnals that meet the spheroid surface in the points S_1 and S_2. This pair separates the isopycnals that do not meet the spheroid surface from those that do. The baroclinically induced flow on account of diffusive isopycnal tilting has been known for a long time, having originally been proposed in the oceanic context where the induced flow has a boundary layer character on account of the dominance of inertia
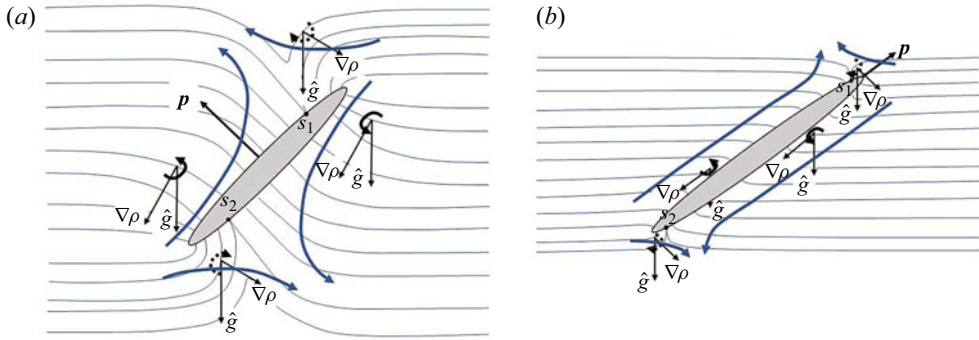
Figure 4. Baroclinically driven flow, for small *Pe*, that is responsible for the rotation of an (*a*) oblate and a (*b*) prolate spheroid, in a stably stratified ambient. The curved blue arrows denote the sense of the baroclinically induced vorticity in the different quadrants of the fluid domain, with vorticities corresponding to anticlockwise and clockwise senses of rotation being denoted by solid and dashed lines; the blue contours denote the deformed isopycnals around each of the spheroids.

(Phillips 1970; Wunsch 1970). Such a flow has also been examined in a Stokesian scenario more recently (Anis Alias & Page 2017), although only for the case of a horizontal circular cylinder wherein symmetry precludes a torque contribution. That there must be a torque on an inclined spheroid, due to the aforementioned baroclinic flow, is obvious. Although the sense of the torque (broadside-on versus edgewise) is not readily evident, one may nevertheless rationalize the scalings observed for the extreme aspect ratio cases. Figure 3 shows that the angular velocity remains finite in the limit of a flat disk ($\kappa \to 0$) which is consistent with the isopycnals being perturbed in a volume of $O(L^3)$ around the spheroid in this limit, with the density perturbation being $O(\gamma L)$, and the test velocity field $U^{(2)}$ being $O(1)$ in this region; the points S_1 and S_2 remain bounded away from the edges of the flat disk. On the other hand, the angular velocity approaches zero as $O(\xi_0 - 1)$ in the limit of a slender fiber, with the points S_1 and S_2 now moving towards the ends of the fiber. The dominant contribution continues to come from a volume of $O(L^3)$. However, although $U^{(2)}$ is $O[\ln(\xi_0 - 1)]^{-1}$, the density perturbation in this region is algebraically small. The slender fiber only perturbs the isopycnals in a thin $O(d^2 L)$ shell around itself, with the density perturbation being $O(\gamma d)$ in this region. Further, each cross-section of the fiber acts as a 2D concentration dipole, implying that the density perturbation decays as $O(1/r)$ for r much greater than d, and is therefore $O(\gamma d)(d/L)$ for $r \sim O(L)$. Using these estimates, and dividing by the $O[\ln(\xi_0 - 1)]^{-1}$ rotational resistance for a slender fiber leads to the aforementioned scaling for the fiber rotation due to the hydrodynamic contribution of the stratification torque.

4.1.1. *A closer look at the Pe ≪ 1 analysis*

Although the $O(Ri_v)$ angular velocity given by (4.7) was said to be valid for small *Pe*, there are, in fact, multiple contributions to the stratification-induced rotation for $Pe \ll 1$; the more detailed arguments herein, and the analysis in Appendix B, yield a precise estimate of the *Pe* interval of validity. Although the dominant contribution to (4.7) arose from buoyancy forces on length scales of $O(L)$, as we show in § 4.2, the dominant length scale contributing to the hydrodynamic component of the stratification torque changes to $O(LRi_v^{-1/3})$ with increasing *Pe*; one therefore expects the singular effect of convection to already be evident for small but finite *Pe*. To see this, we note that, for

933 A17-16

small *Pe*, in addition to the density perturbation driven by the no-flux condition on the spheroid surface that has been analysed in section (4.1), an independent contribution arises from perturbation of the ambient stratification on much larger length scales due to weak convection effects. To obtain an estimate for this latter torque contribution, we consider the correction to the leading-order density perturbation, now denoted as $\rho'^{(10)}$, in a manner similar to the velocity field examined at the end of the earlier section; thus, one writes $\rho'^{(1)} = \rho'^{(10)} + Pe\,\rho'^{(11)}$, with $\nabla^2\rho'^{(11)} \sim \boldsymbol{u}'^{(1)} \cdot \hat{\boldsymbol{g}}$. With $\boldsymbol{u}'^{(1)} \sim 1/r$ on length scales smaller than $O(LRe^{-1})$, one obtains $\rho'^{(11)} \sim r$. The stratification torque at the next order is proportional to $Ri_v Pe \int \rho'^{(11)}\hat{\boldsymbol{g}}\boldsymbol{u}^{(2)}\,\mathrm{d}V$, which turns out to diverge as $O(r^2)$, on using the above estimate for $\rho'^{(11)}$. Cutting off the divergence at the small-*Pe* stratification screening length of $O[L(Ri_v Pe)^{-1/4}]$ (List 1971; Ardekani & Stocker 2010) would seem to lead to an $O(Ri_v Pe)^{1/2}$ torque contribution. However, it is shown in Appendix B that this contribution is identically zero, on account of the fore–aft symmetry of the disturbance density field on scales of $[L(Ri_v Pe)^{-1/4}]$ (Ardekani & Stocker 2010; Varanasi & Subramanian 2021).

The fore–aft asymmetry of the density perturbation, necessary for a non-trivial torque contribution, requires inclusion of the $O(Pe)$ convective term $(\boldsymbol{u} \cdot \nabla\rho')$ in (2.12). It is well known that, for small but finite *Pe*, this convective term becomes comparable to the diffusive term on length scales of $O(LPe^{-1})$, the mass/heat transfer analogue of the inertial screening length (Leal 1992), and the angular velocity scaling therefore depends on the relative magnitudes of the convective (LPe^{-1}) and stratification $(L(Ri_v Pe)^{-1/4})$ screening lengths, which in turn depends on the relative magnitudes of *Pe* and $Ri_v^{1/3}$; this criterion being analogous to the classification into Stokes $(Re \ll Ri_v^{1/3})$ and inertia $(Re \geq Ri_v^{1/3})$ stratification regimes based on the structure of the large-*Pe* disturbance velocity field (Mehaddi *et al.* 2018; Varanasi & Subramanian 2021), except that *Pe* now replaces *Re*. For $Pe \ll Ri_v^{1/3}$, fore–aft asymmetric buoyancy forces acting on scales of $O[L(Ri_v Pe)^{-1/4}]$ lead to an $O(Ri_v^{1/4}Pe^{5/4})$ hydrodynamic torque contribution, an exact expression for which is obtained in Appendix B. In the opposite limit of $Pe \gg Ri_v^{1/3}$, the dominant contribution to the torque integral arises on scales of $O(Ri_v^{-1/3})$, and the resulting torque comes out to be $O(Ri_v^{2/3})$. Thus, the arguments above, and those in Appendix B, show that, for small *Pe*, in addition to the $O(Ri_v)$ torque contribution given by (4.8) and (4.9), there exists a second independent contribution that increases with *Pe* as $O(Ri_v^{1/4}Pe^{5/4})$ for $Pe \ll Ri_v^{1/3}$, but is independent of *Pe*, being $O(Ri_v^{2/3})$ for $Ri_v^{1/3} \ll Pe \ll 1$. This far-field hydrodynamic contribution, arising from a weak convective distortion of the stratified ambient, can evidently exceed the hydrostatic contribution, possibly leading to an edgewise settling regime even for small *Pe*. In light of this additional contribution, the dominance of the $O(Ri_v)$ hydrostatic contribution and the prevalence of broadside-on settling requires $Ri_v \gg Ri_v^{1/4}Pe^{5/4}$, which translates to the stricter criterion $Pe \ll Ri_v^{3/5} \ll 1$, instead of $Pe \ll 1$, as assumed originally.

It is important to point out that the $O(Ri_v)$ scaling in (3.6), (3.7) and (4.7) implies that the associated (dimensional) angular velocities are independent of *U*. Although this must be the case for the hydrostatic contributions, it turns out to be the case for the hydrodynamic component too, at small *Pe*, because the leading-order density perturbation arises as a diffusive response, and is therefore independent of the ambient flow. Despite this *U*-independence, the torque associated with (4.7) does have a hydrodynamic character, in that it still arises from the flow induced by buoyancy forces. Using the $O(\gamma L)$ density perturbation produced by the diffusive response, one obtains a buoyancy-driven velocity

scale of $O(\gamma L^3 g/\mu)$, implying a spheroidal angular velocity of $O(\gamma L^2 g/\mu)$; the latter is $O(Ri_v)$ in units of U/L, this being the scale used in the reciprocal theorem formulation in § 2. Importantly, the U-independence implies that this torque contribution is not necessarily limited to small Ri_v. Instead, it is limited by the assumption of a quasi-steady density perturbation set up on scales of $O(L)$ by diffusion alone, which requires an appropriate Péclet number (based on the aforementioned $O(\gamma L^3 g/\mu)$ velocity scale) to be small; an analogously defined Reynolds number must also be small for the baroclinic flow to be obtained from the Stokes equations. These two requirements translate to $Ri_v Pe, Ri_v Re \ll 1$, which also ensures that the spheroid rotation may be neglected when deriving the disturbance fields. Thus, (4.7) remains valid even when $Ri_v \sim O(1)$ provided $Re, Pe \ll 1$. Note, however, that a genuine dependence, of the hydrodynamic component of the angular velocity contribution, on U arises due to contributions from the outer region, and an estimate of this contribution was obtained in the preceding paragraph (also see Appendix B).

To summarize then, for sufficiently small Pe, all three contributions in (2.22) have a regular character, and therefore, the same dependence on the spheroid orientation, namely $\sin \psi \cos \psi$ with ψ being the angle between $\boldsymbol{p}$ and $\boldsymbol{g}$ as defined above; the Pe interval of validity depends on Ri_v, being $Pe \ll 1$ for $Ri_v \sim O(1)$, and $Pe \ll Ri_v^{3/5}$ for $Ri_v \ll 1$. The inertial contribution is $O(Re)$, whereas both hydrodynamic and hydrostatic components of the stratification contribution are $O(Ri_v)$, with the hydrodynamic component alone acting to orient the spheroid edgewise for prolate spheroids of arbitrary κ and oblate spheroids with $\kappa > 0.41$. Therefore, oblate spheroids with $\kappa < 0.41$ will certainly orient broadside-on for $Pe \ll 1$. Further, it is seen from figures 2 and 3 that the hydrodynamic component always remains smaller in magnitude than the hydrostatic one in the edgewise-rotation regime and, therefore, a sedimenting spheroid, either prolate or oblate, is expected to settle in the broadside-on configuration, regardless of κ, for sufficiently small Pe.

4.2. *The angular velocity due to the hydrodynamic torque in the convection-dominant limit ($Pe \gg 1$)*

In contrast to the small Pe limit examined in the previous section, for $Pe \gg 1$, the dominant contribution to the integral for the stratification-induced hydrodynamic torque in (2.21) comes from length scales of $O(LRi_v^{-1/3})$, the stratification screening length in the Stokes stratification regime ($Re \ll Ri_v^{1/3} \ll 1$). To see this, we note from the right-hand side of the advection diffusion equation (2.16) that, for large Pe, the density perturbation is driven by the convection of the base-state stratification of order unity by the vertical component of the Stokeslet field, $u_3'^{(1)}$. As $u_3'^{(1)} \sim O(1/r)$, one finds $\rho'^{(1)} \sim O(1)$ for $r \gg 1$. This, along with the far-field $O(1/r^2)$ decay of the test velocity field, implies that the integrand in the stratification torque integral decays as $O(1/r^2)$, and that the volume integral therefore diverges as $O(r)$. This divergence is expected to be resolved only when the slow $O(1/r)$ decay of the Stokeslet is accelerated by stratification that, for large Pe, occurs on length scales of $O(LRi_v^{-1/3})$. It has recently been shown in Varanasi & Subramanian (2021) that, for a sedimenting sphere at large Pe, the density and velocity fields are indeed asymptotically small on length scales larger than $O(Ri_v^{-1/3})$, except within a horizontal wake whose vertical extent grows as $O(r_t^{2/5})$, r_t being the distance in the plane transverse to gravity, where the density and axial velocity perturbation decay as $r_t^{-12/5}$ and $r_t^{-14/5}$, respectively; and a buoyant jet in the rear where $u_3'^{(1)}$ reverses sign,

but continues to exhibit an $O(1/r)$ Stokesian decay. Despite the latter slow decay, the asymptotically narrow character of the buoyant jet implies that the torque integral does converge on length scales of $O(LRi_v^{-1/3})$, and is $O(Ri_v^{-1/3})$. The pre-factor of Ri_v in front of the integral in (2.21) implies that the torque and the angular velocity scale as $O(Ri_v^{2/3})$ for $Pe \to \infty$.

As the dominant contribution to the torque integral comes from length scales much larger than $O(L)$, of $O(LRi_v^{-1/3})$, the calculation requires one to rewrite the integral involving $\rho'^{(1)}$, in (2.21), in outer coordinates (defined below), with the sedimenting spheroid in problem 1 now regarded as a point force, and the rotating spheroid in the test problem acting as a combination of rotlet and stresslet singularities (see Marath & Subramanian 2017). The details of this calculation are provided below; a similar calculation, but for low Pe, with the outer region being characterized by a length scale of $O(Ri_v Pe)^{-1/4}$, has been given in Appendix B and the resulting $O(Ri_v^{1/4}Pe^{5/4})$ torque contribution was discussed above in § 4.1.1.

Before delving into the large-Pe analysis, it is worth noting that a reciprocal theorem formulation to determine the stratification-induced correction to the force (that would include both drag and lift components for an arbitrarily oriented spheroid) would involve the test problem of a translating spheroid instead. As the test velocity field now decays as $O(1/r)$ in the far-field, this would lead to a stronger $O(r^2)$ divergence of the force integral, leading to a scaling of $O(Ri_v^{-2/3})$ on truncation of the divergence and, thence, an $O(Ri_v^{1/3})$ stratification-induced correction to the Stokes drag. Such a correction was originally calculated for a spherical particle by Zvirin & Chadwick (1975). A similar calculation was done by Candelier *et al.* (2014) for the small-Pe regime, the drag contribution from the outer region now being $O(Ri_v Pe)^{1/4}$; a later effort has connected this outer-region drag calculation across the different asymptotic regimes (Mehaddi *et al.* 2018). In a very recent study, Dandekar *et al.* (2020) have examined the force and torque acting on an arbitrarily shaped particle sedimenting in a linearly stratified ambient. For anisotropic particles lacking a handedness (that includes the spheroids examined here), the authors find a correction to the force at $O(Ri_v^{1/3})$ similar to the case of a spherical particle mentioned above efforts, but end up not finding a torque at this order, a result that is not surprising in light of the above scaling arguments which show the torque to be $O(Ri_v^{2/3})$. Within the framework of the matched asymptotics expansions approach used by the said authors, the $O(Ri_v^{1/3})$ correction to the drag appears as a response of the particle to an 'ambient uniform flow' that is the limiting form of the outer solution in the matching region ($1 \ll r \ll Ri_v^{-1/3}$); the uniformity of this flow is consistent with the absence of a torque at this order. Incidentally, the existence of an inertial torque induced by a uniform flow suggests a higher $O(ReRi_v^{1/3})$ inner-region contribution to the leading $O(Re)$ inertial angular velocity, in response to the aforementioned $O(Ri_v^{1/3})$ uniform flow that would again orient the spheroid broadside-on; this is in addition to the outer-region correction obtained in § 3, and is dominant in the Stokes stratification regime.

As mentioned above, the stratification torque integral in (2.22) needs to be evaluated in outer coordinates which are related to the coordinates in the particle-fixed reference frame as $\tilde{x} = Ri_v^{1/3}x$, so an $O(1)$ change in $\tilde{x}$ corresponds to x changing by an amount of order the stratification screening length. However, as originally shown by Childress (1964) and Saffman (1965), a Fourier space approach turns out to be much more convenient for a calculation involving the outer region, and we therefore consider the Fourier transformed

equations of continuity and motion, and the advection diffusion equation for the density field, obtained from (2.14)–(2.16), and given by

$$k_i \hat{u}_i'^{(1)} = 0, \tag{4.10}$$

$$-4\pi^2 k^2 \hat{u}_i'^{(1)} - 2\pi i k_i \hat{p}'^{(1)} = -Ri_v(\hat{\rho}'^{(1)} \hat{g}_i) + \tilde{F}\hat{g}_i, \tag{4.11}$$

$$2\pi i k_j \hat{U}_j \hat{\rho}'^{(1)} = \hat{u}_j'^{(1)} \hat{g}_j + \frac{1}{Pe} 4\pi^2 k^2 \hat{\rho}'^{(1)} + \frac{1}{Pe} i 2\pi k_i D_i^s, \tag{4.12}$$

for problem 1. Here, we have used the definition $\hat{f}(k) = \int \mathrm{d}x \exp(-2\pi i k \cdot x) f(x)$ for the Fourier transform, and the sedimenting spheroid has been replaced by a point force, $\tilde{F}\delta(x)$, on the right-hand side of the physical space equations of motion, namely (2.15), with $\tilde{F} = \tilde{F}\hat{g}$, $\tilde{F}$ being the non-dimensional buoyant force (in units of $\mu U L$) exerted by the spheroid; the corresponding dimensional expression has been given in § 2 (given that U is itself defined in terms of F, this re-scaling of F merely amounts to multiplication by X_A). Note that the inertial term in the original equation of motion, (2.15), has now been omitted in (4.11) because, as argued earlier, the leading $O(Re)$ inertial torque is dominated by the inner region, with the outer region contribution being only $O(Re^2 \ln Ri_v^{-1/3})$ (see the end of § 3), and not considered here. Further, on large length scales relevant to the outer region, the spheroid, on account of the no-flux boundary condition at its surface, appears as a concentration-dipole forcing in the advection–diffusion equation. In physical space, this corresponds to a term of the form $D^s \cdot \nabla \delta(x)$, and the Fourier transform of this term appears on the right-hand side of (4.12); D^s here is the *Pe*-dependent strength of the dipole forcing; this can be neglected for the same reason as the inertial term above, its contribution being asymptotically small compared with that arising from the distortion of the base-state stratification (the first term on the right-hand side of (4.12)).

Setting $Pe = \infty$ in (4.12), one obtains

$$\hat{\rho}'^{(1)} = \frac{\hat{u}_j'^{(1)} \hat{g}_j}{2\pi i (k_l \hat{U}_l)}. \tag{4.13}$$

Using (4.13) in (4.11), and operating on both sides with $(\delta_{ij} - \hat{k}_i \hat{k}_j)$ to eliminate the pressure field, one obtains

$$4\pi^2 k^2 \hat{u}_i'^{(1)} = Ri_v \hat{g}_j (\delta_{ij} - \hat{k}_i \hat{k}_j) \frac{\hat{u}_l'^{(1)} \hat{g}_l}{2\pi i (k_p \hat{U}_p)} + \tilde{F}\hat{g}_j (\delta_{ij} - \hat{k}_i \hat{k}_j). \tag{4.14}$$

Contracting with $\hat{g}$ gives

$$\hat{u}_i'^{(1)} \hat{g}_i = \frac{\tilde{F}\hat{g}_i \hat{g}_j (\delta_{ij} - \hat{k}_i \hat{k}_j)}{\left[4\pi^2 k^2 - Ri_v \frac{\hat{g}_m \hat{g}_n (\delta_{mn} - \hat{k}_m \hat{k}_n)}{2\pi i (k_l \hat{U}_l)} \right]}, \tag{4.15}$$

which, on using in (4.13), yields the following final expression for $\hat{\rho}'^{(1)}$:

$$\hat{\rho}'^{(1)}(k) = \frac{\tilde{F}[1 - (\hat{k}_i \hat{g}_i)^2]}{\{8\pi^3 i k^3 (\hat{k}_n \hat{U}_n) - Ri_v [1 - (\hat{k}_m \hat{g}_m)^2]\}}, \tag{4.16}$$

which will be used in the Fourier-space torque integral that is defined below.

933 A17-20

The test velocity field $u_i^{(2)} = U_{ij}^{(2)} \Omega_j^{(2)}$ satisfies the Stokes equations, with the rotating spheroid, on length scales of $O(LRi_v^{-1/3})$, acting as a force-dipole singularity that includes both stresslet and rotlet contributions. Thus, the equations of motion may be written in the form (see Marath & Subramanian 2017):

$$\frac{\partial^2 u_i^{(2)}}{\partial x_j^2} - \frac{\partial p^{(2)}}{\partial x_i} = S_{ij}^{(2)} \frac{\partial}{\partial x_j}[\delta(\boldsymbol{x})], \qquad (4.17)$$

where

$$S_{ij}^{(2)} = B_1[(\epsilon_{ilm}\Omega_l^{(2)} p_m)p_j + (\epsilon_{jlm}\Omega_l^{(2)} p_m)p_i] + B_3 \epsilon_{ijk}\Omega_k^{(2)} \qquad (4.18)$$

with

$$B_1 = \frac{8\pi}{\xi_0^3(-3\xi_0 + 3\coth^{-1}\xi_0(1+\xi_0^2))}, \qquad (4.19)$$

$$B_3 = \frac{8\pi(1-2\xi_0^2)}{\xi_0^3(-3\xi_0 + 3\coth^{-1}\xi_0(1+\xi_0^2))}, \qquad (4.20)$$

for prolate spheroids. There is an additional contribution that is neglected in (4.18), on account of the test spheroid rotating about an axis transverse to $\boldsymbol{p}$, that is, because $\boldsymbol{\Omega}^{(2)} \cdot \boldsymbol{p} = 0$. The term proportional to B_3 in (4.18) is the rotlet singularity (due to transverse rotation), whereas that involving B_1 is the stresslet singularity. Thus, for $\xi_0 \to \infty$, $B_3 = -4\pi$ and B_1 is $O(1/\xi_0^2)$, consistent with a rotating sphere acting as a pure rotlet singularity; note that $B_3 = Y_C/2$, the latter being the resistance function mediating the torque–angular velocity relation for transverse rotation defined earlier.

Fourier transforming (4.17), and contracting with the projection operator $(\boldsymbol{I} - \hat{\boldsymbol{k}}\hat{\boldsymbol{k}})$, one obtains

$$\hat{u}_i^{(2)} = -\frac{\mathrm{i}}{2\pi k}\{B_1[(\epsilon_{mqr}\Omega_q^{(2)} p_r)p_n + (\epsilon_{nqr}\Omega_q^{(2)} p_r)p_m] + B_3\epsilon_{mnq}\Omega_q^{(2)}\}\hat{k}_n(\delta_{im} - \hat{k}_i\hat{k}_m), \qquad (4.21)$$

so the second-order tensor $\boldsymbol{U}^{(2)}$ is given by

$$U_{ij}^{(2)}(\boldsymbol{k}) = -\frac{\mathrm{i}}{2\pi k}\{B_1[(\epsilon_{mjr}p_r)p_n + (\epsilon_{njr}p_r)p_m] + B_3\epsilon_{mnj}\}\hat{k}_n(\delta_{im} - \hat{k}_i\hat{k}_m). \qquad (4.22)$$

Now, using the convolution theorem, the integral for the angular velocity contribution due to the hydrodynamic component of the stratification-induced torque in (2.21) may be written as

$$Ri_v \int \rho'^{(1)}\hat{g}_j U_{ji}^{(2)} \, \mathrm{d}V = Ri_v \int \mathrm{d}\boldsymbol{k}\hat{\rho}'^{(1)}(\boldsymbol{k})\hat{g}_j U_{ji}^{(2)}(-\boldsymbol{k}), \qquad (4.23)$$

where, in applying the convolution theorem, we have assumed the volume integral on the left-hand side of (4.23) to extend over the entire domain, and thereby, neglected the $O(L^3)$ volume of the spheroid. As the dominant contribution arises from length scales of $O(LRi_v^{-1/3})$, this neglect only amounts to an error of $O(Ri_v)$ in the torque integral, and $O(Ri_v^2)$ in the resulting angular velocity.

Using (4.16) and (4.22) in the Fourier space torque integral in (4.23), and after some simplification which includes defining a rescaled wave vector $2\pi \boldsymbol{k}$, one obtains the angular velocity induced by the hydrodynamic stratification torque as

$$\Omega_i^{(1)d} = Ri_v \frac{\mathrm{i}\tilde{F}}{8\pi^3 Y_C} \int \mathrm{d}\boldsymbol{k} \frac{[1 - (\hat{k}_x \hat{g}_x)^2]}{\{\mathrm{i}k^3(\hat{k}_y \hat{U}_y) - Ri_v[1 - (\hat{k}_z \hat{g}_z)^2]\}k} \left[B_1 \left\{ (\epsilon_{irj} p_r \hat{g}_j)(\hat{k}_m p_m) \right. \right.$$
$$\left. \left. + (\epsilon_{irj} p_r \hat{k}_j)(\hat{g}_m p_m) - 2(\hat{k}_m \hat{g}_m)(\hat{k}_j p_j)(\epsilon_{irl} p_r \hat{k}_l) \right\} + B_3 \epsilon_{ijr} \hat{g}_j \hat{k}_r \right], \tag{4.24}$$

the terms proportional to B_1 and B_3 being the stresslet and rotlet-induced torque contributions, respectively. Redefining the new wave vector to be $Ri_v^{-1/3} \boldsymbol{k}$, so it remains of order unity on length scales of order the stratification screening length (and, thereby, pertains to the outer region in Fourier space), and considering only the real part of the integral above, one obtains

$$\Omega_i^{(1)d} = Ri_v^{2/3} \frac{\tilde{F}}{8\pi^3 Y_C} \left[B_1 \int \mathrm{d}\boldsymbol{k} \frac{[1 - (\hat{k}_x \hat{g}_x)^2]k^2(\hat{k}_v \hat{U}_v)}{\{k^6(\hat{k}_y \hat{U}_y)^2 + [1 - (\hat{k}_z \hat{g}_z)^2]^2\}} [\{(\epsilon_{irj} p_r \hat{g}_j)(\hat{k}_m p_m) \right.$$
$$+ (\epsilon_{irj} p_r \hat{k}_j)(\hat{g}_m p_m) - 2(\hat{k}_m \hat{g}_m)(\hat{k}_j p_j)(\epsilon_{irl} p_r \hat{k}_l)\}]$$
$$\left. + B_3 \int \mathrm{d}\boldsymbol{k} \frac{[1 - (\hat{k}_x \hat{g}_x)^2]k^2(\hat{k}_v \hat{U}_v)}{\{k^6(\hat{k}_y \hat{U}_y)^2 + [1 - (\hat{k}_z \hat{g}_z)^2]^2\}} \epsilon_{ijr} \hat{g}_j \hat{k}_r \right], \tag{4.25}$$

where the angular velocity due to the hydrodynamic stratification torque finally comes out to be $O(Ri_v^{2/3})$, as anticipated by the scaling arguments above, and the convergent Fourier integrals in (4.25) are evaluated below; note that the imaginary part of (4.24), neglected in (4.25), may be shown to equal zero by symmetry. Before evaluating the integrals above using a specific coordinate system, we note that the force–velocity relationship for a sedimenting spheroid, for the scalings used here, is given by

$$\hat{U}_i = \left[p_i p_j + \frac{X_A}{Y_A}(\delta_{ij} - p_i p_j) \right] \hat{g}_j. \tag{4.26}$$

Defining the aspect-ratio-dependent resistance ratio $An(\kappa) = X_A/Y_A$, equation (4.26) may be written as

$$\hat{U}_i = [(1 - An)p_i p_j + An\delta_{ij}]\hat{g}_j. \tag{4.27}$$

where An decreases monotonically from unity for a sphere to a minimum of $1/2$ for an infinitely slender prolate spheroid ($\kappa \to \infty$); on the oblate side, An increases from unity to a maximum of $3/2$ for a flat disk ($\kappa \to 0$). Both of these may be readily verified based on the expressions given in Appendix A.

To evaluate the above Fourier integrals, we choose a spherical coordinate system with its polar axis along $\hat{U}$. Interestingly, a numerical evaluation in the alternate and perhaps more natural choice of a $\hat{g}$-aligned coordinate system turns out to much more involved, with the individual integrals making up the torque diverging as $Pe^{1/2}$ in the limit $Pe \to \infty$, the divergence arising due to the buoyant jet mentioned above, and that corresponds to the region $\hat{\boldsymbol{k}} \cdot \hat{\boldsymbol{U}} = 0$, $k \ll 1$ in Fourier space (see Varanasi & Subramanian 2021). We have verified that the divergences of the individual contributions cancel out, and the total torque integral is nevertheless convergent and independent of Pe for $Pe \to \infty$,

matching the result obtained below in the $\hat{U}$-aligned system. In the latter coordinate system, $\hat{U} = U_m \mathbf{1}_U$, $\mathbf{1}_U$ being the unit vector along $\hat{U}$; using (4.27), one finds $U_m = \cos^2 \psi + An^2 \sin^2 \psi$, ψ being the angle between $\hat{g}$ and p defined in earlier sections. The unit wave vector is given by $\hat{k} = \sin \theta \cos \phi \mathbf{1}_{U^{\perp 1}} + \sin \theta \sin \phi \mathbf{1}_{U^{\perp 2}} + \cos \theta \mathbf{1}_U$, with $\mathbf{1}_{U^{\perp 1}}$ chosen to lie in the plane of sedimentation, that is, the plane containing the vectors p, $\hat{U}$ and $\hat{g}$, so the torque acting on the spheroid points along $\hat{g} \wedge \hat{p} = \mathbf{1}_{U^{\perp 2}}$. With this choice, $\hat{k} \cdot \hat{U} = U_m \cos \theta$. We take $p = \cos \psi_U \mathbf{1}_U + \sin \psi_U \mathbf{1}_{U^{\perp 1}}$, ψ_U being the angle between p and $\hat{U}$. Noting from (4.27) that $\hat{U} \cdot p = \hat{g} \cdot p$, one has $\cos \psi_U = \cos \psi / U_m$. With ψ_U as defined above, $\hat{k} \cdot p = \cos \psi_U \cos \theta + \sin \psi_U \sin \theta \cos \phi$, and $\hat{k} \cdot \hat{g} = An^{-1}[\hat{k} \cdot \hat{U} - (1 - An) \cos \psi \hat{k} \cdot p]$. As mentioned above, the torque only has a component along $\mathbf{1}_{U^{\perp 2}}$ in the chosen coordinate system. As the vectors involved in the integrals in (4.25) are $\hat{g} \wedge \hat{k}$, $p \wedge \hat{g}$ and $p \wedge \hat{k}$, we have

$$\epsilon_{2jr} \hat{g}_j \hat{k}_r = \frac{1}{An} [U_m \sin \theta \cos \phi - (1 - An) \cos \psi (\cos \psi_U \sin \theta \cos \phi - \sin \psi_U \cos \theta)],$$
(4.28)

$$\epsilon_{2jr} p_j \hat{g}_r = -\frac{U_m \sin \psi_U}{An},$$
(4.29)

$$\epsilon_{2jr} p_j \hat{k}_r = - \sin \psi_U \cos \theta + \cos \psi_U \sin \theta \cos \phi,$$
(4.30)

which defines all quantities involved in the calculation. Using these expressions in the integrals in (4.25), the k-integration is carried out analytically while the remaining two angular integrals are evaluated numerically using Gaussian quadrature. From (4.28)–(4.30), and other quantities defined in the preceding text, the ψ-dependence of the large-Pe hydrodynamic angular velocity is seen to be more complicated than the $\cos \psi \sin \psi$ dependence obtained earlier for the inertial and hydrostatic contributions in § 3, and for the hydrodynamic component, in the limit $Pe \ll Ri_v^{3/5}$, in § 4.1. This is along expected lines because the large-Pe limit examined in this section is a singular perturbation problem, as evident from the outer region contributing at leading order (this aspect is also seen in the outer-region contribution to the torque at low Pe, derived in Appendix B). Another feature of the singular character is that, unlike the earlier torque contributions, the large-Pe hydrodynamic stratification torque is in general a non-separable function of ψ and κ.

Figures 5(a) and 6(a) show plots of the angular velocity ($\Omega^{(1)d}$), due to the hydrodynamic component of the stratification torque, versus ψ for prolate and oblate spheroids, respectively. As evident from figure 5(a), for prolate spheroids, the magnitude of the angular velocity is expectedly small in the near-sphere limit, increasing monotonically with κ to a (finite) maximum in the limit of a slender fiber. Figures 5(b) shows plots of the angular velocity scaled with the square of the eccentricity (ξ_0^{-2}), so as to obtain a collapse in the near-sphere limit. Note that the finite value of the stratification-induced angular velocity in the limit of a slender fiber ($\xi_0 \to 1$) is in contrast to the $O[\ln(\xi_0 - 1)]^{-1}$ scaling exhibited by the inertial angular velocity calculated in § 3 (see also Dabade *et al.* 2015), and implies that, for fixed Re and Ri_v, the stratification torque invariably becomes dominant for large aspect ratios. Figure 6(b) confirms the squared-eccentricity scaling for oblate spheroids with near-unity aspect ratios; expectedly, the angular velocity approaches a finite value in the limit of a flat disk. Importantly, for
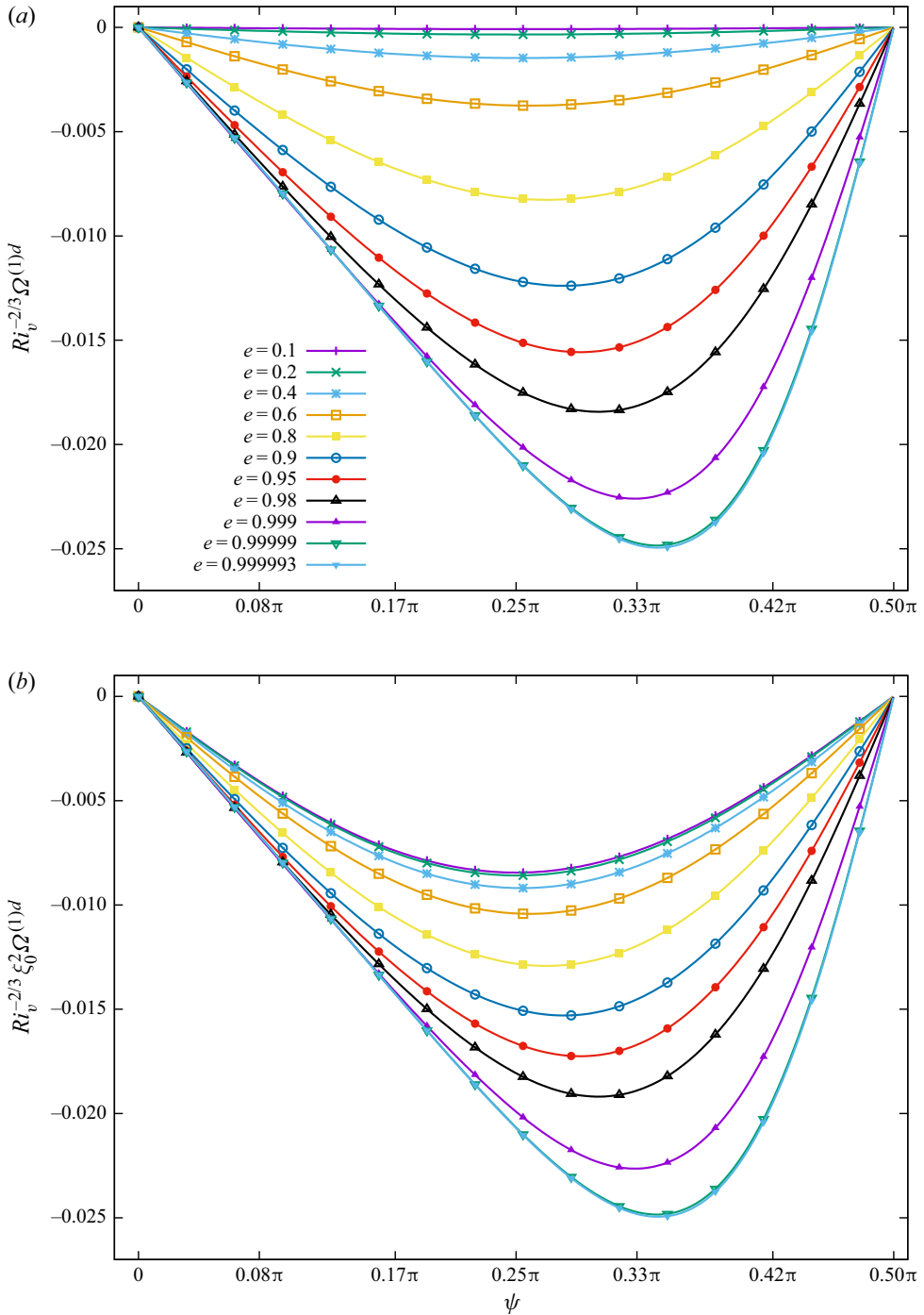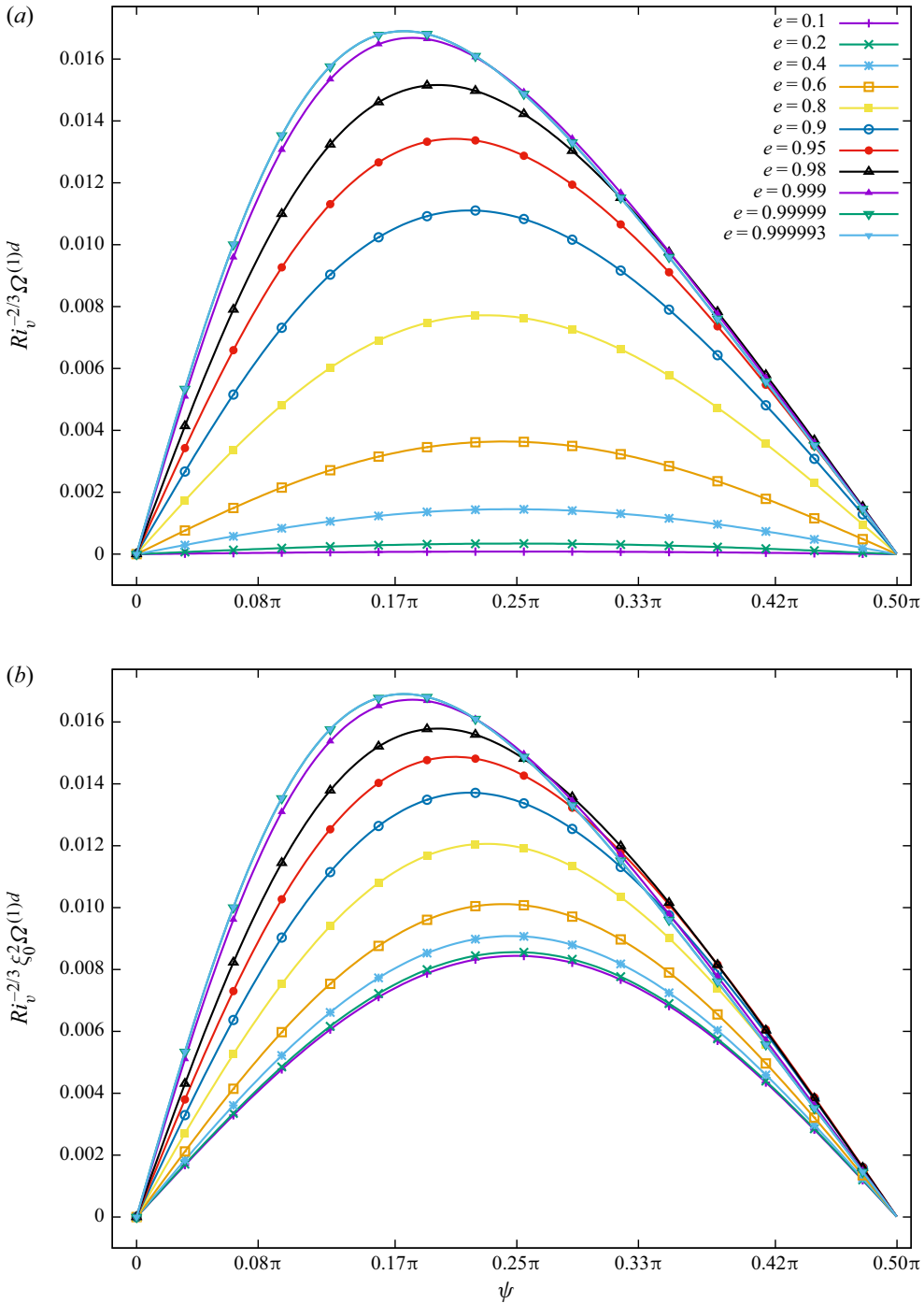
Figure 5. The scaled angular velocity ($Ri_v^{-2/3} \Omega^{(1)d}$), due to the hydrodynamic component of the stratification torque, for prolate spheroids of different aspect ratios: (*a*) $Ri_v^{-2/3} \Omega^{(1)d}$, for prolate spheroids, as a function of the spheroid inclination with gravity; (*b*) $Ri_v^{-2/3} \Omega^{(1)d}$, normalized by the near-sphere scaling ($1/\xi_0^2$) for prolate spheroids, plotted as a function of the spheroid inclination with gravity.

Figure 6. The scaled angular velocity ($Ri_v^{-2/3}\Omega^{(1)d}$), due to the hydrodynamic component of the stratification torque, for oblate spheroids of different aspect ratios: (*a*) $Ri_v^{-2/3}\Omega^{(1)d}$, for oblate spheroids, as a function of the spheroid inclination with gravity; (*b*) $Ri_v^{-2/3}\Omega^{(1)d}$, normalized by the near-sphere scaling ($1/\xi_0^2$) for oblate spheroids, plotted as a function of the spheroid inclination with gravity.
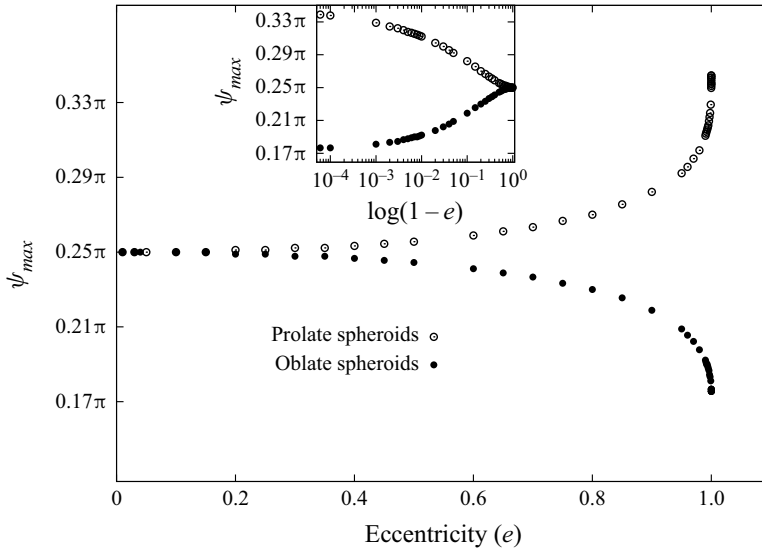
Figure 7. The angle corresponding to the maximum angular velocity, arising from the hydrodynamic component of the stratification torque, plotted as a function of the spheroid aspect ratio (both prolate and oblate spheroids); the inset shows the variation of this angle on a log–log scale, emphasizing the approach to finite values for extreme aspect ratios ($\kappa = 0$ and ∞).

both prolate and oblate spheroids, the sign of $\Omega^{(1)d}$ is such as to rotate the spheroid onto an edgewise orientation.

The non-trivial orientation dependence of the angular velocity referred to in the previous paragraph is also evident from the plots in figures 5(a) and 6(a). For near-unity aspect ratios, the angular velocity curve is nearly symmetric about $\psi = \pi/4$; that the angular dependence in this limit is indeed of the form $\sin\psi\cos\psi$ may be shown based on the fact that for $An \to 1$, $\psi_U \approx \psi$. The asymmetry about $\psi = \pi/4$ increases as the aspect ratio departs from unity, with the location of the maximum angular velocity moving to ψ greater than and less than $\pi/4$ for prolate and oblate spheroids, respectively, as shown in figure 7. To see the deviation of the angular dependence from the aforementioned simple form more clearly, in figures 8(a) and 8(b) we plot the angular velocity, scaled by the inertial angular velocity which is proportional to $\sin\psi\cos\psi$, again as a function of ψ. For near-unity aspect ratios, one obtains a horizontal line, while for both larger and smaller aspect ratios, this renormalized angular velocity asymptotes from one plateau for $\psi \to 0$ to a second one for $\psi \to \pi/2$.

4.2.1. *A closer look at the Pe ≫ 1 analysis*

In contrast to the inertial contribution determined in § 3, which was independent of the ambient stratification at leading order, the stratification-induced torque can, in principle, be coupled to inertial forces even in the limit $Re, Ri_v \ll 1$. For sufficiently small Pe ($Pe \ll Ri_v^{3/5}$ as argued in § 4.1.1), the density perturbation that determines the stratification torque arises from a diffusive response to the no-flux condition on the surface of the sedimenting spheroid, and is therefore independent of the fluid motion. As a result, a non-trivial coupling between stratification and inertia occurs primarily for large Pe. As the dominant length scales contributing to the stratification torque in this limit are much larger than $O(L)$, the magnitude of the density perturbation is controlled by the
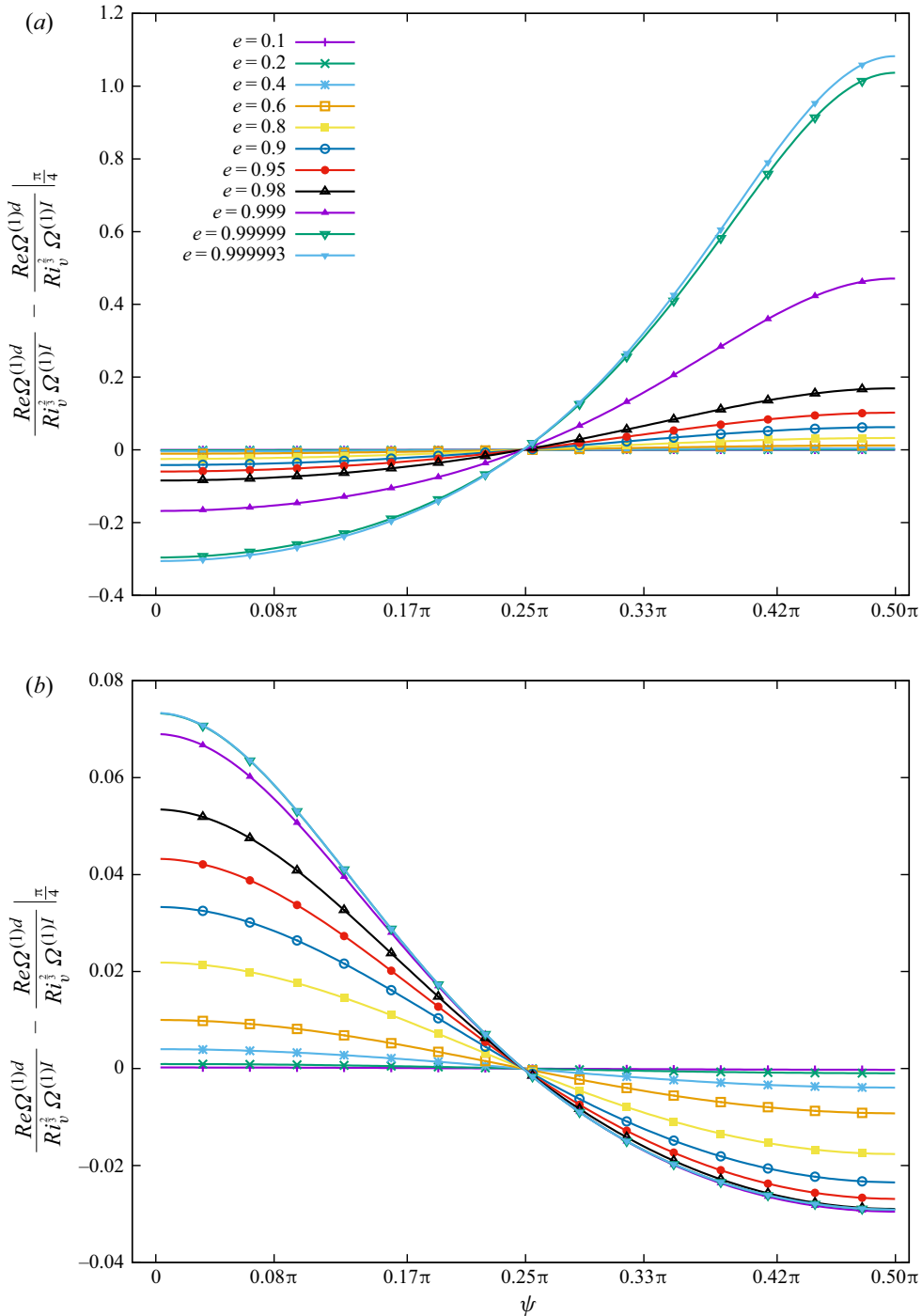
933 A17-26

Figure 8. Ratio of the angular velocities due to the hydrodynamic stratification and inertial torques: (*a*) prolate spheroid; (*b*) oblate spheroid. The stratification-induced rotation is higher for the near-vertical and near-horizontal orientations for prolate and oblate spheroids, respectively; note that the angular velocity ratio at $\psi = \pi/4$ has been subtracted for convenient depiction.

convection of the ambient stratification by the far-field disturbance fluid motion. The nature of this convection is, therefore, dependent on the form of the disturbance velocity field, and this in turn depends on the relative magnitudes of the inertial (LRe^{-1}) and stratification ($LRi_v^{-1/3}$) screening lengths. The calculation of the angular velocity due to the hydrodynamic stratification torque detailed above pertains to the Stokes stratification regime, with $Re \ll Ri_v^{1/3}$, where the disturbance velocity field directly transitions from the Stokeslet form to a more rapid decay on length scales of $O(LRi_v^{-1/3})$ (Varanasi & Subramanian 2021) and is therefore independent of Re. In the Stokes stratification regime, therefore, the stratification-induced rotation, both in the limit of small and large Pe, is independent of Re, and the inertial and stratification angular velocity contributions are additive. This will no longer true when $Re \geq O(Ri_v^{1/3})$, corresponding to the so-called inertia-stratification regime, in which case the leading-order stratification-induced rotation for large Pe will be a function of $Re/Ri_v^{1/3}$. In the limit $Ri_v^{1/3} \ll Re \ll 1$, opposite to that analysed above, the disturbance velocity transitions from an $O(1/r)$ to an $O(1/r^2)$ decay (outside of a viscous wake) across length scales of order the inertial screening length. This leads to the stratification torque integrand decaying as $O(1/r^3)$ for length scales much larger than $O(LRe^{-1})$, and the torque integral in (2.22) continues to exhibit a logarithmic divergence. This (milder) divergence is only eliminated when buoyancy forces become comparable to inertial forces at a secondary screening length that was estimated in Varanasi & Subramanian (2021) to be $O(Re/Ri_v)^{1/2}$. Accounting for the aforementioned cut-off of the logarithmic divergence, the angular velocity arising from the hydrodynamic stratification torque is expected to have a leading $O[Ri_v Re^{-1} \ln(Re/Ri_v^{1/3})]$ contribution arising from a region between the primary and secondary screening lengths (that is, due to the logarithmic growth for $Re^{-1} \ll r \ll (Re/Ri_v)^{1/2}$), with logarithmically smaller $O(Ri_v Re^{-1})$ contributions arising from length scales of order the two screening lengths. Assuming this angular velocity to rotate the spheroid towards an edgewise configuration, and equating it to the $O(Re)$ inertial contribution, one obtains $Re \leq Ri_v^2$ for a transition to an edgewise-settling regime. This, however, contradicts the requirement $Re \gg Ri_v^{1/3}$ characterizing the inertia-stratification regime, implying that the inertial angular velocity contribution remains dominant in this regime. Thus, one concludes that, in the limit of small Re and Ri_v, a broadside-on–edgewise transition is possible only in the Stokes stratification regime.

To end this subsection, we again examine the validity of a quasi-steady state assumed in the analysis above for large Pe. As already argued in § 3, momentum diffusion occurs asymptotically fast for small Re and, therefore, the quasi-steady assumption used to evaluate the stratification torque integral relies on the time scale for the density disturbance to approach a steady state being much shorter than that characterizing spheroid rotation. The former time scale may be regarded as that required to convect the density perturbation through the $O(LRi_v^{-1/3})$ stratification screening length, and is therefore $O(L/URi_v^{-1/3})$. The time scale of rotation is $O(L/URe^{-1})$ or $O(L/URi_v^{-2/3})$, depending on which of Re or $Ri_v^{2/3}$ is greater. In either case the time scale for the development of a steady density perturbation is smaller, provided one remains in the Stokes stratification regime $Re \ll Ri_v^{1/3} \ll 1$. Note that the perturbation density field, for $Pe = \infty$, is expected to be logarithmically singular along the rear stagnation streamline, as has been shown for the case of a spherical particle (see Varanasi & Subramanian 2021), with this singularity either being resolved on a larger diffusive time scale (that is, due to Pe being regarded as large but finite), or on account of the unsteadiness arising from the rotation of the settling spheroid.

However, the convergence of the Fourier integrals involved in the stratification torque above implies that the contribution of the transiently developing region in the immediate neighbourhood of the rear stagnation streamline is irrelevant as far as the leading-order hydrodynamic stratification torque is concerned, and a quasi-steady analysis of this torque remains valid for $Re \ll Ri_v^{1/3}$.

5. Results and discussion

In earlier sections, we have derived expressions for the angular velocity of a spheroid settling in a viscous linearly stratified ambient. The spheroid angular velocity is the sum of three components; the inertial and hydrostatic contributions are given by (3.3) and (3.6) [(3.4) and (3.7)] for prolate [oblate] spheroids; the hydrodynamic contributions arising from the stratification are given by (4.8) and (4.9) for prolate and oblate spheroids, respectively, in the limit of small *Pe*; and are obtained from the numerical evaluation of (4.25) for $Pe \gg 1$. As already argued in § 4.1, both prolate and oblate spheroids will settle broadside-on for sufficiently small *Pe* regardless of κ. Herein, we therefore focus on the transition from broadside-on to edgewise settling that becomes possible for large *Pe*. In this limit, the hydrodynamic stratification component is $O(Ri_v^{2/3})$ and rotates the spheroid towards an edgewise orientation regardless of κ. It is dominant over the $O(Ri_v)$ hydrostatic component that favours the broadside-on orientation. Thus, the transition from broadside-on to edgewise settling, at leading order, depends on the relative magnitudes of the inertial and hydrodynamic stratification angular velocities, and for a fixed κ, the transition threshold is determined by the ratio $Ri_v/Re^{3/2}$ in the limit $Re, Ri_v \ll 1$. However, the differing orientation dependence of the inertial and stratification angular velocities, as evident from figure 8(*a*), for instance, implies that the transition cannot be characterized by $Ri_v/Re^{3/2}$ equalling a single κ-dependent threshold. An instance of the latter scenario, that of a single threshold demarcating differing orientation dynamics regimes, occurs when the competing physical effects are inertia and viscoelasticity, both of which lead to angular velocities with a $\sin\psi\cos\psi$ dependence, so that the edgewise and broadside-on settling regimes are demarcated by a single critical curve in the $De/Re - \kappa$ plane, *De* here being the Deborah number, a dimensionless measure of elasticity (see Dabade *et al.* 2015).

Writing the leading-order hydrodynamic stratification component in the general form $Ri_v^{2/3}F_s(\kappa, \psi)$, for large *Pe*, and equating it to the inertial component, of the form $ReF_I(\kappa)\sin\psi\cos\psi$, the threshold criterion for the broadside-on–edgewise transition is determined by the ratio $Ri_v/Re^{3/2} = [(\sin\psi\cos\psi)F_I(\kappa)/F_s(\kappa, \psi)]^{3/2}$. Recall from figure 8 that, for all $\kappa > 1$ ($\kappa < 1$), $F_s(\kappa, \psi)/(F_I(\kappa)\sin\psi\cos\psi)$ approaches its minimum and maximum values for $\psi \to 0(\pi/2)$ and $\pi/2(0)$, respectively, varying monotonically in between these limits. Now, define $(Ri_v/Re^{3/2})_{max} = \lim_{\psi\to 0(\psi\to\pi/2)}[(F_I(\kappa)\sin\psi\cos\psi)/F_s(\kappa, \psi)]^{3/2}$ and $(Ri_v/Re^{3/2})_{min} = \lim_{\psi\to(\pi/2)(\psi\to 0)}[(F_I(\kappa)\sin\psi\cos\psi)/F_s(\kappa, \psi)]^{3/2}$ for prolate (oblate) spheroids, both of which are finite and only functions of κ. One then has the following behaviour for the orientation of either a sedimenting prolate or an oblate spheroid. For $Ri_v/Re^{3/2} < (Ri_v/Re^{3/2})_{min}$, the broadside-on orientation is the only equilibrium; likewise, for $Ri_v/Re^{3/2} > (Ri_v/Re^{3/2})_{max}$ the longside-on orientation is the only equilibrium. For $Ri_v/Re^{3/2}$ between the aforementioned thresholds, the inertial and stratification angular velocity curves must intersect at an orientation, ψ_i (say), intermediate between 0 and $\pi/2$. It is easily seen that this equilibrium is a stable one for both the prolate and oblate cases;
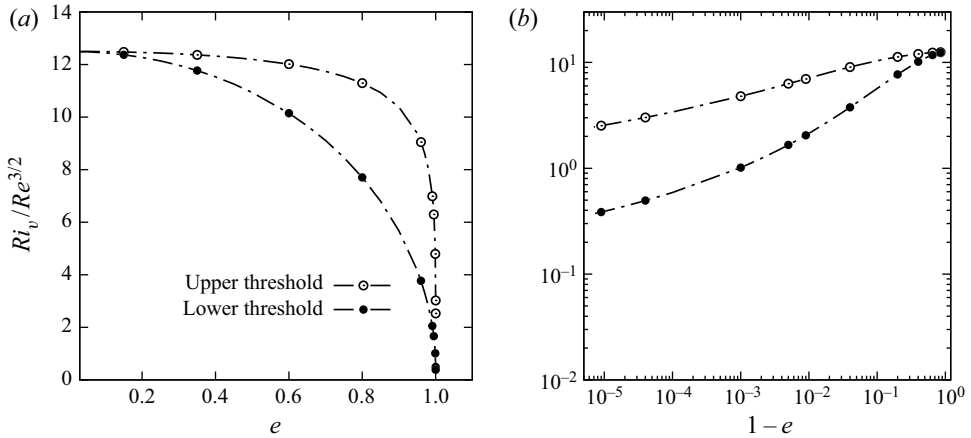
Figure 9. The upper and lower threshold curves that demarcate the regimes of broadside-on settling (below), edgewise settling (above) and intermediate equilibrium orientations (in between), plotted as a function of eccentricity, for a prolate spheroid; the plot on the right presents a magnified view of the thresholds near the slender-fiber limit.

for example, in the prolate case, the stratification-induced angular velocity is greater than the inertial one for $\psi_i < \psi < \pi/2$, with the converse being true $0 < \psi_i < \psi$, implying that a prolate spheroid with its orientation in either of these intervals is rotated towards $\psi = \psi_i$. As $Ri_v/Re^{3/2}$ increases from the lower $[(Ri_v/Re^{3/2})_{min}]$ to the upper threshold $[(Ri_v/Re^{3/2})_{max}]$, the intermediate equilibrium orientation, ψ_i, decreases from $\pi/2$ to zero. Figures 9 and 10 show the aforementioned pair of threshold curves, $(Ri_v/Re^{3/2})_{min}(\kappa)$ and $(Ri_v/Re^{3/2})_{max}(\kappa)$, plotted in the $Ri_v/Re^{3/2} - \kappa$ plane for prolate and oblate spheroids, respectively. Both the threshold values in figure 9 approach zero in the limit of large aspect ratios because, as already noted in § 4.2, the stratification-induced torque remains finite in this limit, in contrast to the inertial torque which becomes logarithmically small (see figure 1). As seen from the log–log plot in figure 9, the convergence of the thresholds to zero is slow on account of the aforementioned logarithmic scaling. For oblate spheroids, the lower and upper thresholds approach distinct finite values in the limit of a flat disk. As the angular velocity due to the hydrodynamic stratification torque approaches a $\sin \psi \cos \psi$ dependence for $\kappa \to 1$ from either the prolate or oblate side, the two threshold curves towards a common albeit finite critical value in the near-sphere limit in both figures 9 and 10. In effect, for a prolate spheroid, the thresholds diverge from a common finite value for $\kappa = 1$, tending to a maximum separation for $\kappa \approx 4.11$ ($e \approx 0.94$), before approaching zero in the limit $\kappa \to \infty$. For flat disks, the threshold curves diverge away monotonically from a common value as κ increases from unity, approaching a maximum separation in the limit of a flat disk.

In order to connect to experiments, we now discuss the implication of the aforementioned predictions, within a quasi-steady framework, for a spheroid that starts off with an arbitrary initial orientation and sediments through a stratified fluid at large *Pe*; arguments in §§ 4.1 and 4.2 show that the quasi-steady assumption remains rigorously valid in the Stokes stratification regime, regardless of *Pe*, provided *Re* and Ri_v are small. The experiments reported in Mercier *et al.* (2020) correspond to an ambient linear stratification that includes a neutral buoyancy level. The latter would correspond to the equilibrium location of the sedimenting spheroid for long times, and for the viscous overdamped regime under consideration, one expects the spheroid velocity U to decrease
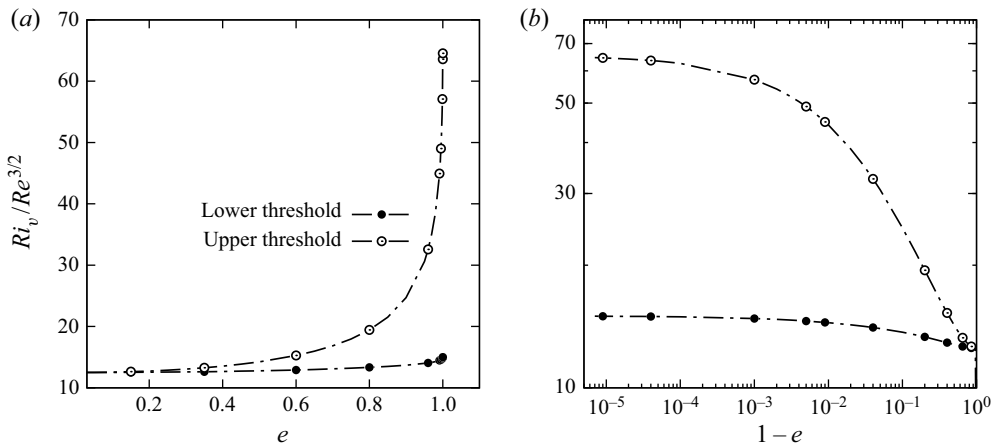
Figure 10. The upper and lower threshold curves that demarcate the regimes of broadside-on settling (below), edgewise settling (above) and intermediate equilibrium orientations (in between), plotted as a function of eccentricity, for an oblate spheroid; the plot on the right presents a magnified view of the thresholds near the flat-disk limit.

monotonically to zero as it approaches this level. In dimensionless terms, Re and Pe decrease with time, whereas Ri_v increases with time. If the spheroid starts off sufficiently far above neutral buoyancy level, then the initial terminal velocity is likely large enough for the ratio $Ri_v/Re^{3/2} \sim U^{-5/2}$ to be below the lower κ-dependent threshold in figure 10 (note that the particles used in the experiments were disk-shaped, and maybe likened to thin oblate spheroids). As a result, the spheroid starts off rotating towards a broadside-on orientation. The spheroid will slow down as it approaches the neutral buoyancy level, and the resulting increase in $Ri_v/Re^{3/2}$ will eventually cause it to exceed the aforementioned lower threshold, leading to the broadside-on orientation becoming an unstable equilibrium. Assuming the spheroid to have had sufficient time prior to this point, to have already attained a near-broadside-on orientation, one expects the onset of a reversal in rotation. Strictly speaking, the arguments in the previous paragraph, with regard to the existence of an intermediate stable equilibrium, only pertain to a truly steady setting (where the neutral buoyancy level corresponds to an infinitely great depth). For the experimental scenario, assuming a sufficiently slow increase in $Ri_v/Re^{3/2}$ with time, the spheroid would progress quasi-statically through a sequence of intermediate orientation equilibria, on its way to an edgewise configuration. Finally, in the immediate neighbourhood of the neutral buoyancy level, the dynamics would appear to be slow enough for one to be in the small-Pe regime analysed in § 4.1, and the resulting dominance of the hydrostatic component of the stratification torque, over the $O(Ri_v)$ hydrodynamic component, should again reverse the spheroid rotation, causing it to finally approach its equilibrium location in a broadside-on configuration. The aforementioned sequence of events is broadly consistent with the observations in Mercier *et al.* (2020). Note that because $U \to 0$ for long times in the vicinity of the neutral buoyancy level, Ri_v becomes arbitrarily large in the vicinity of the neutral buoyancy level, in turn leading to an apparent breakdown of the analysis. As discussed in § 4.1.1, the expressions (4.8) and (4.9), for the hydrodynamic component of the stratification angular velocity remain valid, even for Ri_v of order unity or greater provided $Ri_v Pe \ll 1$ (for sufficiently small Re). The magnitude of $Ri_v Pe$, which is independent of U, therefore determines whether the small-Pe analysis remains valid close to the neutral buoyancy level. For large $Ri_v Pe$, the small-Pe screening length of

$O[L(Ri_v Pe)^{-1/4}]$ would be much less than L, implying that the baroclinic flow driving spheroid rotation is likely restricted to a thin boundary layer on the surface of the spheroid, this boundary-layer character being similar to the original analysis of Phillips (1970); the resulting magnitude of the hydrodynamic stratification component is not known. It must also be emphasized that both Re and Ri_v for the disks in the said experiments are of order unity, and a direct quantitative comparison with the experimental trajectories is therefore not possible. Such a comparison would require the analogues of the thresholds in figures 9 and 10 for finite Re and Ri_v; even within the asymptotic framework analysed here, there exist corrections of $O(Ri_v^{1/3})$ to the threshold $Ri_v/Re^{3/2}$ values in the said figures, owing to the neglect of both the $O(Ri_v)$ hydrostatic contribution, and higher-order corrections to the hydrodynamic contribution.

The experiments reported in Mrokowska (2018), Mrokowska (2020b) and Mrokowska (2020a) correspond to a nonlinearly stratified ambient where the density varies within an intermediate layer sandwiched between homogeneous upper and lower layers. The effects of the stratification on particle orientation, and the resulting coupling to the settling velocity via the orientation-dependent resistance coefficient, lead to extrema (both maxima and minima) in the settling velocity profile; five different phases have been identified in the settling behaviour of thin disks. A detailed theoretical investigation to establish the variation of the settling velocity profile for small Re and Ri_v requires an integration of the coupled translational and orientational equations of motion, and this will be reported separately. It is worth noting one interesting feature in these experiments, however. The particles used in the experiments have a density that is greater than that of the lower denser layer of the nonlinearly stratified ambient, and the resulting absence of a neutral buoyancy level renders these experiments closer to the ideal steady-state scenario of a constant U, thereby pointing to the possible relevance of the intermediate orientation equilibria identified in figures 9 and 10. Interestingly, Mrokowska (2020b) observed thick disks to behave differently from thin ones. On entering the transition layer, these disks appear to rotate from an initial broadside-on configuration, attained in the upper layer, towards an intermediate inclined orientation, before rotating back onto a broadside-on orientation in the lower homogeneous layer. The persistence of the inclined orientation in the transition layer appears consistent with the prediction of equilibrium orientations in figure 10. The ratio $Ri_v/Re^{3/2}$ equals $(\gamma L^{3/2} \mu^{1/2} g)/(U^{5/2} \rho_0^{3/2})$ in terms of the underlying physical parameters. Further, using the scale $F/(\mu L X_A)$ for U, one obtains the ratio as $(3X_A/4\pi)^{5/2}(\gamma \mu^3/((\rho_0 g)^{3/2}(\Delta\rho)^{5/2} L b^{5/2}))$. Both the thick and thin disks used in the experiments of Mrokowska (2020b) correspond to $\kappa \ll 1$, implying that $X_A(\kappa) \approx X_A(0)$ in the expression for $Ri_v/Re^{3/2}$ above. It is therefore the thickness b that varies significantly in going from the thin to the thick disk in the experiments, and the $b^{-5/2}$ scaling of the above ratio implies that the thick disk will correspond to a significantly lower value of $Ri_v/Re^{3/2}$. Thus, it is possible for the thin disk to correspond to an $Ri_v/Re^{3/2}$ above the upper threshold, with the thick disk falling in between the two thresholds above; in this sense, our predictions again appear broadly consistent with the observations in Mrokowska (2020b).

6. Conclusions and future work

To summarize, in this study, we present the first rigorous theoretical description of the orientation dynamics of spheroidal particles in a stably stratified ambient. The stratification-induced hydrodynamic torque, acting on a spheroidal particle, has been calculated for the first time. For large Pe in particular, the torque is shown to rotate

both prolate and oblate spheroids towards an edgewise orientation regardless of aspect ratio. The theoretical predictions with regard to the transitions between broadside-on and edgewise settling, and with regard to the existence of intermediate inclined equilibrium orientations, appear broadly consistent with very recent experiments. Unfortunately, and as already mentioned in § 5, a detailed quantitative comparison appears out of reach at the moment; the particles used in all of the experiments, referred to in § 5, correspond to Ri_v and Re values of order unity and higher. The quantitative disconnect between experiment and theory is also evident from the threshold Froude number condition identified by Mercier *et al.* (2020) for the so-called perfect disk which, translated to our notation, corresponds to a threshold Ri_v/Re^3; as opposed to the ratio $Ri_v/Re^{3/2}$ identified in § 5. We therefore hope that future experiments will use smaller particles, in an attempt to access the regime of small Re and Ri_v, and thereby validate the detailed predictions given here. It needs to be emphasized that the many of the smaller zooplankton, for typical values of the stratification pertaining to the oceanic pycnocline, correspond to the small Re–Ri_v regime, and thus the theoretical framework given here is certainly relevant to natural settings (the oceanic realm in particular).

It is worth mentioning that the focus in the present manuscript has been on the large-*Pe* analysis, in an attempt to explain the transition between broadside-on and edgewise settling observed in experiments, all of which correspond to a salt-stratified ambient, and for the millimetre-sized particles used, pertain therefore to large *Pe*. There are, however, interesting issues that emerge even in the small *Pe* regime.

(i) Scaling arguments given in 4.1.1, and the analysis in Appendix B, highlight the possibility of an analogous broadside-on–edgewise transition in the range $Ri_v^{3/5} < Pe \ll 1$. One expects the parametric combination $(Ri_v^{1/4}Pe^{5/4})/Re$ to determine the transition threshold in the range $Ri_v^{3/5} \ll Pe \ll Ri_v^{1/3}$, with the ratio $Ri_v/Re^{3/2}$ controlling this transition for $Pe \gg Ri_v^{1/3}$. The emergence of an $O(Ri_v^{2/3})$ torque for $Pe \gg Ri_v^{1/3}$ suggests that the large-*Pe* analysis might be applicable to a wider range of *Pe* that initially apparent (see Appendix B).

(ii) The opposing senses of rotation of oblate spheroids, with $\kappa < 0.41$ in the small-*Pe* ($Pe \ll Ri_v^{3/5}$) and large-*Pe* regimes point to a non-trivial dependence of the stratification-induced angular velocity on *Pe*, one that can be examined in detail through a numerical investigation over the entire range of *Pe*.

These aspects will be taken up in future work.

Finally, it is also of interest to move beyond orientation dynamics, towards a more detailed illustration of actual particle trajectories which requires an integration of the quasi-steady equations of motion for both translational and rotational degrees of freedom. This would enable a more comprehensive comparison with the experiments of Mrokowska (2020*b*) and Mrokowska (2020*a*). We expect some of the non-trivial signatures to be revealed in an analysis that might only incorporate an anisotropic Stokes drag for the positional dynamics, a valid leading-order approximation for $Re, Ri_v \ll 1$. This will again be taken up in a future study.

Declaration of interests. The authors report no conflict of interest.

Author ORCIDs.

Ⓓ Ganesh Subramanian https://orcid.org/0000-0003-4314-3602.

Appendix A. Resistance functions and inertial torque

The expressions for $F_I^p(\xi_0)$ and $F_I^o(\xi_0)$ defined in (3.3) and (3.4) are given in terms of the eccentricity of the spheroid ($e = 1/\xi_0$) as

$$
\begin{aligned}
F_I^p(\xi_0) = {} & \frac{-\pi e^2 \left(420e + 2240e^3 + 4249e^5 - 2152e^7\right)}{315((e^2+1)\tanh^{-1} e - e)^2((1-3e^2)\tanh^{-1} e - e)} \\
& + \frac{\pi e^2 \left(420 + 3360e^2 + 1890e^4 - 1470e^6\right)\tanh^{-1} e}{315((e^2+1)\tanh^{-1} e - e)^2((1-3e^2)\tanh^{-1} e - e)} \\
& - \frac{\pi e^2 \left(1260e - 1995e^3 + 2730e^5 - 1995e^7\right)(\tanh^{-1} e)^2}{315((e^2+1)\tanh^{-1} e - e)^2((1-3e^2)\tanh^{-1} e - e)},
\end{aligned} \tag{A1}
$$

and

$$
\begin{aligned}
F_I^o(\xi_0) = {} & \frac{\pi e^3\sqrt{1-e^2}\left(-420 + 3500e^2 - 9989e^4 + 4757e^6\right)}{315\sqrt{1-e^2}(-e\sqrt{1-e^2} + (1+2e^2)\sin^{-1} e)(e\sqrt{1-e^2} + (2e^2-1)\sin^{-1} e)^2} \\
& + \frac{210\pi e^2 \left(2 - 24e^2 + 69e^4 - 67e^6 + 20e^8\right)\sin^{-1} e}{315\sqrt{1-e^2}(-e\sqrt{1-e^2} + (1+2e^2)\sin^{-1} e)(e\sqrt{1-e^2} + (2e^2-1)\sin^{-1} e)^2} \\
& + \frac{105\pi e^3 \left(12 - 17e^2 + 24e^4\right)(\sin^{-1} e)^2}{315(-e\sqrt{1-e^2} + (1+2e^2)\sin^{-1} e)(e\sqrt{1-e^2} + (2e^2-1)\sin^{-1} e)^2}.
\end{aligned} \tag{A2}
$$

The resistance functions X_A, Y_A and Y_C are expressed in terms of the spheroid eccentricity as

$$
X_A = \frac{16\pi e^3}{\left(2e - (1+e^2)\log\left(\dfrac{1+e}{1-e}\right)\right)}, \tag{A3}
$$

$$
Y_A = -\frac{32\pi e^3}{\left(2e + (3e^2 - 1)\log\left(\dfrac{1+e}{1-e}\right)\right)}, \tag{A4}
$$

$$
Y_C = \frac{32\pi e^3(e^2 - 2)}{3\left(-2e + (1+e^2)\log\left(\dfrac{1+e}{1-e}\right)\right)}, \tag{A5}
$$

for a prolate spheroid and as

$$
X_A = -\frac{8\pi e^3}{\left[e\sqrt{1-e^2} + (2e^2 - 1)\cot^{-1}\left(\dfrac{\sqrt{1-e^2}}{e}\right)\right]}, \tag{A6}
$$

$$Y_A = \frac{16\pi e^3}{\left[e\sqrt{1-e^2} - (1+2e^2)\cot^{-1}\left(\frac{\sqrt{1-e^2}}{e}\right) \right]}, \tag{A7}$$

$$Y_C = \frac{16\pi e^3 (e^2 - 2)}{3\left[e\sqrt{1-e^2} - (1-2e^2)\cot^{-1}\left(\frac{\sqrt{1-e^2}}{e}\right) \right]}, \tag{A8}$$

for an oblate spheroid.

Appendix B. Additional convective contributions to the spheroid angular velocity for $Pe \ll 1$

In § 4.1, an $O(Ri_v)$ contribution to the spheroid angular velocity, given by (4.7), arose from the density perturbation driven by the no-flux condition on the spheroid surface (and given by (4.3)). This contribution denotes the effect of buoyancy forces acting in a volume of $O(L^3)$ around the spheroid, and may be termed the inner-region contribution. Herein, we show that there exist additional buoyancy-induced contributions to the spheroid angular velocity arising from a perturbation of the ambient stratification, on much larger length scales, due to weak convection effects. Convection effects become important on length scales of order the stratification screening length of $L(Ri_v Pe)^{-1/4}$ for $Ri_v Pe \ll 1$ (Ardekani & Stocker 2010 and § 4.1.1), and the resulting outer-region contribution may be isolated from the full integral for the hydrodynamic component of the stratification torque in (2.22), by first subtracting the aforementioned inner-region contribution. Thus, we begin from the following difference integral:

$$Ri_v \frac{1}{Y_c} \int (\rho'^{(1)} - \rho'^{(10)})\hat{g}_j U_{ji}^{(2)} \, dV, \tag{B1}$$

where the density disturbance defined by (4.3) is now denoted as $\rho'^{(10)}$ (as in § 4.1.1); the test velocity field tensor $U^{(2)}$ is given in (4.22). Now, recall from § 4.1.1 that the difference $\rho'^{(1)} - \rho'^{(10)}$ grows as $O(Pe\,r)$, leading to the dominant contribution to the difference integral in (B1) arising from scales large compared with $O(L)$, even in the limit $Ri_v Pe \ll 1$. Therefore, neglecting the volume of the spheroid, and applying the convolution theorem, one obtains

$$Ri_v \frac{1}{Y_c} \int (\rho'^{(1)} - \rho'^{(10)})\hat{g}_j U_{ji}^{(2)} \, dV = Ri_v \frac{1}{Y_c} \int [\hat{\rho}'^{(1)}(\boldsymbol{k}) - \hat{\rho}'^{(10)}(\boldsymbol{k})]\hat{g}_j \hat{U}_{ji}^{(2)}(-\boldsymbol{k}) \, d\boldsymbol{k}.$$

$$\tag{B2}$$

The Fourier-transformed density field, $\hat{\rho}'^{(1)}(\boldsymbol{k})$, is obtained by solving (4.10)–(4.12), being given by

$$\hat{\rho}'^{(1)} = \frac{-\tilde{F}Pe[1 - (\hat{g}_m\hat{k}_m)^2] + i8\pi^3 k^2 k_j D_j^s}{\left[iPe8\pi^3 k^2 k_j \hat{U}_j - PeRi_v(1 - (\hat{g}_n\hat{k}_n)^2) - 16\pi^4 k^4 \right]}. \tag{B3}$$

The Fourier-transformed density, $\hat{\rho}'^{(10)}(\boldsymbol{k})$, in (B2) corresponds to the approximate form of $\rho'^{(10)}$ at large distances ($k \ll 1$), and may be obtained from Fourier transforming the

solution of the diffusion equation with a concentration-dipole forcing at the origin (see the discussion after (4.12) in § 4.2); thus, $\hat{\rho}'^{(10)}(\mathbf{k})$ is given by

$$\hat{\rho}'^{(10)} = -\frac{\mathrm{i}2\pi k_j D_j^s}{4\pi^2 k^2}, \tag{B4}$$

where the dipole strength, $\mathbf{D}^s$, is an order unity function of the spheroid aspect ratio for $Pe \ll 1$; it may be shown that $\mathbf{D}^s = D_{1s}\hat{\mathbf{g}} \cdot (\mathbf{I} - \mathbf{pp}) + D_{2s}(\hat{\mathbf{g}} \cdot \mathbf{p})\mathbf{p}$, where $D_{1s} = 8\pi(\xi_0^2 - 1)/3\xi_0^2(-\xi_0^2 + (\xi_0^2 - 1)\xi_0 coth^{-1}\xi_0 + 2)$ and $D_{2s} = 4\pi(\xi_0^2 - 1)/3\xi_0^3(-\xi_0^2 coth^{-1}\xi_0 + \xi_0 + coth^{-1}\xi_0)$ for prolate spheroids; the corresponding expressions for oblate spheroids may be obtained using the transformation presented in § 3.

As the dominant contributions to (B2) come from scales of $O[L(Ri_v Pe)^{-1/4}]$, we define a rescaled Fourier wave vector pertaining to the outer region as $\mathbf{k}_o = (Ri_v Pe)^{-1/4}\mathbf{k}$. On doing so, one finds from (B3) and (B4):

$$\hat{\rho}'^{(1)}(\mathbf{k}_o) - \hat{\rho}'^{(10)}(\mathbf{k}_o)$$
$$= \frac{\tilde{F}[1 - (\hat{g}_m \hat{k}_{om})^2] - Ri_v^{3/4} Pe^{-1/4}\mathrm{i}8\pi^3 k_o{}^2 k_{oj} D_j^s}{Ri_v[-\mathrm{i}Pe^{3/4} Ri_v^{-1/4}8\pi^3 k_o^2 k_{oj}\hat{U}_j + (1 - (\hat{g}_n \hat{k}_{on})^2) + 16\pi^4 k_o^4]} + \frac{\mathrm{i}2\pi k_{oj} D_j^s}{(Ri_v Pe)^{1/4}4\pi^2 k_o^2}. \tag{B5}$$

The relative magnitudes of the first with regards to the remaining terms in the denominator of $\hat{\rho}'^{(1)}(\mathbf{k}_o)$ depends on the ratio $Pe/Ri_v^{1/3}$, as mentioned in § 4.1.1. In the limit $Pe \ll Ri_v^{1/3}$, the density difference in (B5) reduces to

$$\hat{\rho}'^{(1)}(\mathbf{k}_o) - \hat{\rho}'^{(10)}(\mathbf{k}_o) \approx \frac{\tilde{F}[1 - (\hat{g}_m \hat{k}_{om})^2]}{Ri_v[(1 - (\hat{g}_n \hat{k}_{on})^2) + 16\pi^4 k_o^4]}, \tag{B6}$$

at leading order. The test velocity field tensor in (4.22) is again $O(1/k) \sim O[Ri_v Pe)^{-1/4}/k_o]$. Using this along with the $O(Ri_v Pe)^{3/4}$ volume in Fourier space that contributes to the integral in (B2) (that is, $\mathrm{d}\mathbf{k} = (Ri_v Pe)^{3/4}\mathrm{d}\mathbf{k}_o$), would appear to lead to an $O(Ri_v Pe)^{1/2}$ outer-region contribution to the angular velocity for $Ri_v, Pe \ll 1$. This contribution is, however, identically zero on account of the integrand being an odd function of $\mathbf{k}$. The absence of such a contribution arises from the fore–aft symmetry, at leading order, of the density and velocity disturbance fields in the outer region (see Ardekani & Stocker 2010; Varanasi & Subramanian 2021); the symmetry of the density disturbance field may be seen from its Fourier transform in (B6) which is an even function of $\mathbf{k}_o$.

Recall that in § 4.1.1, we had mentioned that the $O(Ri_v)$ inner-region contribution remained valid even for finite Ri_v provided $Ri_v Pe \ll 1$, this because this torque contribution arose from $O(\gamma L^3 g/\mu)$ baroclinic flow induced due to the deformed isopycnals around a stationary spheroid, rather than the $O(U)$ disturbance velocity field associated with translation; the resulting dimensional angular velocity was independent of U. Interestingly, the small-Pe screening length above is also independent of U; it equals $(\mu.D/Lg\gamma)^{1/4}$ in terms of the actual physical parameters. The U-independence suggests that screening length for the onset of buoyancy-induced screening is independent of the source of the disturbance flow; it may indeed by verified, using an $O(\gamma L^3 g/\mu)$ scale for the velocity field and going through the arguments of § 4.1.1, that one obtains the same screening length. However, the more rapid $O(1/r^2)$ decay of the dipolar baroclinic flow

implies that the $O(1/r)$ Stokeslet field dominates the distorts the pycnals at leading order, and it is this contribution that is accounted for in (B6).

In light of the symmetry-induced cancellation at leading order, one needs to consider the correction to (B6) to obtain the leading-order contribution from the outer region. In the limit $Pe \ll Ri_v^{1/3}$, on expanding (B5), one readily finds

$$\hat{\rho}'^{(1)}(\boldsymbol{k}_o) - \hat{\rho}'^{(10)}(\boldsymbol{k}_o) \approx \frac{[\tilde{F}(1 - (\hat{g}_m\hat{k}_{om})^2)]}{Ri_v[(1 - (\hat{g}_n\hat{k}_{on})^2) + 16\pi^4 k_o^4]}$$

$$+ \frac{i2\pi k_{oj}D_j^s[(1 - (\hat{g}_m\hat{k}_{om})^2)]}{(Ri_vPe)^{1/4}[(1 - (\hat{g}_n\hat{k}_{on})^2) + 16\pi^4 k_o^4]4\pi^2 k_o^2} + \frac{Pe^{3/4}i\tilde{F}(1 - (\hat{g}_m\hat{k}_{om})^2)8\pi^3 k_o^2 k_{oj}\hat{U}_j}{Ri_v^{5/4}[(1 - (\hat{g}_n\hat{k}_{on})^2) + 16\pi^4 k_o^4]^2},$$
(B7)

where we have only included correction terms that are odd in $\boldsymbol{k}$ which will lead to a non-zero angular velocity in (B2). On combining the scalings arising from the test velocity $((Ri_vPe)^{-1/4})$, the Fourier space volume $((Ri_vPe)^{3/4})$ and the Ri_v pre-factor in (B2), one finds the first correction term (proportional to $\boldsymbol{D}^s$) in (B7) to lead to an angular velocity of $O(Ri_v^{5/4}Pe^{1/4})$, whereas the second correction term gives a contribution of $O(Ri_v^{1/4}Pe^{5/4})$. The first correction is, however, always smaller than the $O(Ri_v)$ inner-region contribution for $Ri_v, Pe \ll 1$. Therefore, we only consider the second correction for the explicit calculation below. Substituting (B7) into the integral in (B2), one finally obtains the following integral expression:

$$\Omega_i^{(1)d^{outer}} = \frac{Ri_v^{1/4}Pe^{5/4}}{Y_c} \int \frac{i\tilde{F}(1 - (\hat{g}_m\hat{k}_{om})^2)8\pi^3 k_o^2 k_{oj}\hat{U}_j}{[(1 - (\hat{g}_n\hat{k}_{on})^2) + 16\pi^4 k_o^4]^2}\hat{g}_l\hat{U}_{li}^{(2)}(-\boldsymbol{k}_o)\,\mathrm{d}\boldsymbol{k}_o, \qquad \text{(B8)}$$

for the outer-region contribution to the hydrodynamic component of the stratification-induced angular velocity, where

$$U_{ij}^{(2)}(\boldsymbol{k}_o) = -\frac{i}{2\pi k_o}\{B_1[(\epsilon_{mjr}p_r)p_n + (\epsilon_{njr}p_r)p_m] + B_3\epsilon_{mnj}\}\hat{k}_{on}(\delta_{im} - \hat{k}_{oi}\hat{k}_{om}), \qquad \text{(B9)}$$

with B_1 and B_3 being given by (4.19) and (4.20), respectively, for prolate spheroids. The aspect-ratio-dependent functions B_1 and B_3 for oblate spheroids can again be obtained as mentioned above.

To reiterate, the contribution given by (B8) exists in addition to the $O(Ri_v)$ contribution evaluated in § 4.1, and given by (4.7). A comparison for $Ri_v \ll 1$ readily shows that the (B8) is dominant when $Pe \gg Ri_v^{3/5}$. Using (B9) in (B8), one obtains

$$\Omega_i^{(1)d^{outer}}$$

$$= Ri_v^{1/4}Pe^{5/4}\frac{4\pi^2\tilde{F}}{Y_c}\left[B_1\int \frac{(1 - (\hat{g}_m\hat{k}_{om})^2)k_o^2\hat{k}_{oj}\hat{U}_j}{[(1 - (\hat{g}_n\hat{k}_{on})^2) + 16\pi^4 k_o^4]^2}\epsilon_{irj}p_r\{\hat{g}_j(\hat{k}_{ol}p_l) + \hat{k}_{oj}(\hat{g}_lp_l)\right.$$

$$\left. -2(\hat{k}_{ol}p_l)(\hat{k}_{oq}\hat{g}_q)\hat{k}_j\}\,\mathrm{d}\boldsymbol{k}_o + B_3\int \frac{(1 - (\hat{g}_m\hat{k}_{om})^2)k_o^2\hat{k}_{oj}\hat{U}_j}{[(1 - (\hat{g}_n\hat{k}_{on})^2) + 16\pi^4 k_o^4]^2}\epsilon_{ijr}\hat{g}_j\hat{k}_{or}\,\mathrm{d}\boldsymbol{k}_o\right]. \qquad \text{(B10)}$$

The evaluation of the integral in (B10) is best done in a $\hat{\boldsymbol{g}}$-aligned spherical coordinate system. After expressing $\hat{\boldsymbol{U}}$ in terms of $\hat{\boldsymbol{g}}$, $\boldsymbol{p}$ and $An(\kappa)$ as in (4.27), the unit wave vector

$\hat{\boldsymbol{k}}_o$ and $\boldsymbol{p}$ may be written in the form $-\cos\theta'\hat{\boldsymbol{g}} + \sin\theta'\cos\phi'\mathbf{1}_{g\perp 1} + \sin\theta'\sin\phi'\mathbf{1}_{g\perp 2}$ and $-\cos\psi\hat{\boldsymbol{g}} + \sin\psi\mathbf{1}_{g\perp 1}$, respectively, in a $\hat{\boldsymbol{g}}$-aligned coordinate system similar to the $\hat{U}$-aligned coordinate system used in §4.2; θ' and ϕ' here being the polar and azimuthal angles, with the polar axis being along $-\hat{\boldsymbol{g}}$. Substituting these in (B10) and using the rescaled wave vector $2\pi\boldsymbol{k}_o$ leads to the following form:

$$\Omega_2^{(1)d^{outer}}$$

$$= Ri_v^{1/4}Pe^{5/4}\frac{\tilde{F}}{8\pi^3 Y_c}\left[\int_0^\infty \mathrm{d}k_o \int_0^\pi \mathrm{d}\theta' \int_0^{2\pi} \mathrm{d}\phi' \left[(\cos\psi\cos\theta' + \sin\psi\sin\theta'\cos\psi)\right.\right.$$

$$\left.\left. \times \cos\psi(1 - An) + \cos\theta' An\right](B_1 f_1 + B_3 \sin\theta'\cos\phi')\frac{k_o^4\sin^3\theta'}{(k_o^4 + \sin^2\theta')^2}\right], \quad \text{(B11)}$$

$$\Omega_2^{(1)d^{outer}}$$

$$= Ri_v^{1/4}Pe^{5/4}\frac{\tilde{F}}{8\pi^3 Y_c}\frac{\pi^{5/2}\Gamma\left(\frac{9}{4}\right)\sin 2\psi}{231\sqrt{2}\Gamma\left(\frac{3}{4}\right)}[-12AnB_1 - 6(1 - An)B_1 + 11(1 - An)B_3$$

$$+(1 - An)B_1\cos 2\psi)]. \quad \text{(B12)}$$

An explicit calculation shows that the angular velocity given by (B12) always acts to orient the spheroid edgewise, and as mentioned above, is greater than the inner-region contribution for $Pe > Ri_v^{3/5}$. A comparison with the inertial torque obtained in §3 (given by (3.3) and (3.4) for prolate and oblate spheroids) suggests that the broadside-on–edgewise transition may now be characterized on the $Ri_v^{1/4}Pe^{5/4}/Re - \kappa$ plane in the range $Ri_v^{3/5} \ll Pe \ll Ri_v^{1/3}$. Note that the dependence on ψ in (B12) is more complicated than that the $\sin 2\psi$-dependence characterizing the regular contributions derived in §§3 and 4.1. However, the deviation from the $\sin 2\psi$-dependence turns out to be very small in magnitude, and as a result, the upper and lower thresholds, separating the broadside-on and edgewise orientations in the aforesaid parameter plane, are nearly coincident.

The above analysis for the outer-region contribution is restricted to the limit $Pe \ll Ri_v^{1/3}$. In the opposite limit, $Pe \gg Ri_v^{1/3}$, the first term in the denominator in (B5), that denotes the effects of the ambient convection, is dominant over the second term that denotes the buoyancy forces. The first term in the numerator continues to be dominant, and therefore, at leading order, one now obtains

$$\hat{\rho}'^{(1)}(\boldsymbol{k}_o) \approx \frac{\tilde{F}[1 - (\hat{g}_m\hat{k}_{om})^2]}{[-\mathrm{i}(Ri_vPe)^{3/4}8\pi^3 k_o^2 k_{oj}\hat{U}_j + Ri_v 16\pi^4 k_o^4]}. \quad \text{(B13)}$$

The two terms in the denominator, denoting the convection and diffusion of the density disturbance, are comparable when $k_o \sim O(Ri_v^{-1/4}Pe^{3/4})$ which, in physical space, corresponds to the familiar (dimensional) convective screening length of $O(LPe^{-1})$. However, combining this with the test velocity field leads to an integrand that is $O(1/k^4)$ for small k, in turn leading to the Fourier integral in (B2) being divergent for $k \to 0$. This suggests that the dominant contribution in the said limit comes from length scales much larger than $O(Pe^{-1})$. A closer examination shows that, for $Pe \gg Ri_v^{1/3}$, the dominant

contribution to the integral in (B2) arises for $k \sim O(Ri_v^{1/3})$, corresponding to the large-*Pe* stratification screening length of $O(Ri_v^{-1/3})$, and that is indeed much larger than the aforementioned convective screening length; the viscous forces are now asymptotically small compared with the convection and buoyancy terms, so the balance reduces to that considered in § 4.2 for large *Pe*. Thus, the implication is that the angular velocity integral in (B2) reduces to the same one as that obtained in § 4.2 when $Pe \gg Ri_v^{1/3}$, and the outer-region contribution is now $O(Ri_v^{2/3})$. The extended range of validity of the large-*Pe* analysis for the torque mirrors the drag scenario where the analysis of Zvirin & Chadwick (1975) was found to be valid for a larger interval of *Pe* than originally anticipated (Mehaddi *et al.* 2018).

To summarize, for *Pe* small compared with unity, the hydrodynamic component of the stratification-induced angular velocity always includes an inner-region contribution of $O(Ri_v)$ that has been derived in § 4.1, with an additional outer-region contribution that is $O(Ri_v^{1/4} Pe^{5/4})$ for $Pe \ll Ri_v^{1/3}$, being given by (B12) above, and that is $O(Ri_v^{2/3})$ for $Pe \gg Ri_v^{1/3}$, the corresponding expression being the same as that obtained in § 4.2. The only difference between the angular velocity contributions in the regimes $Ri_v^{1/3} \ll Pe \ll 1$ and $Pe \gg 1$ is that, although sub-dominant, there is still an $O(Ri_v)$ inner-region contribution in the former case owing to the dominance of diffusion on length scales of $O(L)$; in contrast, diffusion is only expected to be important in a boundary layer with a thickness of $O(Pe^{-1/3})$ for $Pe \gg 1$, and there can be no analogue of the small-*Pe* $O(Ri_v)$ contribution.

Appendix C. Spheroidal harmonics solutions

In (3.1) and (3.2), $S_{t,s}^{(3)}$ and $S_{t,s}^{(2)}$ denote the decaying (biharmonic and harmonic) vectorial solutions of the Stokes equations in spheroidal coordinates, and are given by the following expressions:

$$S_{1,0}^{(3)} = \left[(x_1 \mathbf{1}_1 + x_2 \mathbf{1}_2 + x_3 \mathbf{1}_3) \frac{\partial}{\partial x_3} Q_0^0(\xi) - \left(Q_0^0(\xi) + \mathrm{d}\xi_0^2 \left(\frac{\partial}{\partial x_3} \left[Q_1^0(\xi) P_1^0(\eta) \right] \right) \right) \mathbf{1}_3 \right.$$

$$\left. - \mathrm{d}(\xi_0^2 - 1) \left(\mathbf{1}_1 \frac{\partial}{\partial x_1} \left[Q_1^0(\xi) P_1^0(\eta) \right] + \mathbf{1}_2 \frac{\partial}{\partial x_2} \left[Q_1^0(\xi) P_1^0(\eta) \right] \right) \right], \tag{C1}$$

$$S_{1,1}^{(3)} - S_{1,-1}^{(3)} = \left[-2 \left((x_1 \mathbf{1}_1 + x_2 \mathbf{1}_2 + x_3 \mathbf{1}_3) \frac{\partial Q_0^0(\xi)}{\partial x_1} - Q_0^0(\xi) \mathbf{1}_1 \right) \right.$$

$$\left. -\mathbf{1}_3 \, \mathrm{d}\xi_0^2 \frac{\partial}{\partial x_3} (P_1^1(\eta) Q_1^1(\xi) \cos\phi) - \mathrm{d}(\xi_0^2 - 1) \left(\mathbf{1}_1 \frac{\partial}{\partial x_1} + \mathbf{1}_2 \frac{\partial}{\partial x_2} \right) (P_1^1(\eta) Q_1^1(\xi) \cos\phi) \right], \tag{C2}$$

$$S_{1,1}^{(2)} + S_{1,-1}^{(2)} = \left[2 P_1^0(\eta) Q_1^0(\xi) \mathbf{1}_1 + P_1^1(\eta) Q_1^1(\xi) \cos(\phi) \mathbf{1}_3 \right], \tag{C3}$$

$$S_{2,1}^{(3)} - S_{2,-1}^{(3)} = \left[(x_1 \mathbf{1}_1 + x_2 \mathbf{1}_2 + x_3 \mathbf{1}_3) \frac{\partial}{\partial x_3} (P_1^1(\eta) Q_1^1(\xi) \sin(\phi)) - \frac{\mathrm{d}\xi_0^2}{3} \right.$$

$$\left. \frac{\partial}{\partial x_3} (P_2^1(\eta) Q_2^1(\xi) \cos(\phi)) \mathbf{1}_3 - \frac{\mathrm{d}(\xi_0^2 - 1)}{3} \left(\mathbf{1}_1 \frac{\partial}{\partial x_1} + \mathbf{1}_2 \frac{\partial}{\partial x_2} \right) (P_2^1(\eta) Q_2^1(\xi) \cos(\phi)) \right], \tag{C4}$$

with the $P_t^s(\eta)$ and $Q_t^s(\xi)$ being the associated Legendre functions of the first and second kind, respectively (for $s = 0$, the $P_t^s(\eta)$ correspond to the usual Legendre polynomials). We have the following expressions for the Q_t^s involved in (C1)–(C4):

$$Q_0^0(\xi) = \coth^{-1}\xi, \tag{C5}$$

$$Q_1^0(\xi) = \xi\coth^{-1}\xi - 1, \tag{C6}$$

$$Q_1^1(\xi) = \left(\bar{\xi}^2\coth^{-1}\xi - \xi\right)/\bar{\xi}, \tag{C7}$$

$$Q_2^1(\xi) = (-3\xi^2 + 3\bar{\xi}^2\xi\coth^{-1}\xi + 2)/\bar{\xi}. \tag{C8}$$

Further, $P_1^0(\eta) = \eta$, $P_1^1(\eta) = \bar{\eta}$ and $P_2^1(\eta) = 3\eta\bar{\eta}^2$. The general expressions for the vector spheroidal harmonics $\boldsymbol{S}_{t,s}^{(3)}$, for arbitrary t and s, have been obtained in the solid mechanics context, and are given in Kushch (1997) and Kushch (1998).

REFERENCES

ANAND, P., RAY, S.S. & SUBRAMANIAN, G. 2020 Orientation dynamics of sedimenting anisotropic particles in turbulence. *Phys. Rev. Lett.* **125**, 034501.

ANIS ALIAS, A.M. & PAGE, M.A. 2017 Low-Reynolds-number diffusion-driven flow around a horizontal cylinder. *J. Fluid Mech.* **825**, 1035–1055.

ARDEKANI, A.M. & STOCKER, R. 2010 Stratlets: low Reynolds number point-force solutions in a stratified fluid. *Phys. Rev. Lett.* **105** (8), 084502.

AUGUSTE, F., MAGNAUDET, J. & FABRE, D. 2013 Falling styles of disks. *J. Fluid Mech.* **719**, 388–405.

CANDELIER, F., MEHADDI, R. & VAUQUELIN, O. 2014 The history force on a small particle in a linearly stratified fluid. *J. Fluid Mech.* **749**, 184–200.

CHILDRESS, S. 1964 The slow motion of a sphere in a rotating, viscous fluid. *J. Fluid Mech.* **20** (2), 305–314.

COLE, M., PENNIE, L., HALSBAND, C. & GALLOWAY, T.S. 2011 Microplastics as contaminants in the marine environment: a review. *Mar. Pollut. Bull.* **62**, 2588–2597.

DABADE, V., MARATH, N.K. & SUBRAMANIAN, G. 2015 Effects of inertia and viscoelasticity on sedimenting anisotropic particles. *J. Fluid Mech.* **778**, 133–188.

DABADE, V., MARATH, N.K. & SUBRAMANIAN, G. 2016 The effect of inertia on the orientation dynamics of anisotropic particles in simple shear flow. *J. Fluid Mech.* **791**, 631–703.

DANDEKAR, R., SHAIK, V.A. & ARDEKANI, A.M. 2020 Motion of an arbitrarily shaped particle in a density stratified fluid. *J. Fluid Mech.* **890**, A16.

DOOSTMOHAMMADI, A. & ARDEKANI, A.M. 2013 Interaction between a pair of particles settling in a stratified fluid. *Phys. Rev.* E **88**, 023029.

DOOSTMOHAMMADI, A. & ARDEKANI, A.M. 2014 Reorientation of elongated particles at density interfaces. *Phys. Rev.* E **90** (3), 033013.

DOOSTMOHAMMADI, A., DABIRI, S. & ARDEKANI, A.M. 2014 A numerical study of the dynamics of a particle settling at moderate Reynolds numbers in a linearly stratified fluid. *J. Fluid Mech.* **750**, 5–32.

DOOSTMOHAMMADI, A., STOCKER, R. & ARDEKANI, A.M. 2012 Low-Reynolds-number swimming at pycnoclines. *Proc. Natl Acad. Sci.* **109** (10), 3856–3861.

GUILLAUME, M. & MAGNAUDET, J. 2002 Path instability of a rising bubble. *Phys. Rev. Lett.* **88** (1), 014502.

GUSTAVSSON, K., SHEIKH, M.Z., LOPEZ, D., NASO, A., PUMIR, A. & MEHLIG, B. 2019 Effect of fluid inertia on the orientation of a small prolate spheroid settling in turbulence. *New J. Phys.* **21**, 083008.

HANAZAKI, H. 1988 A numerical study of three-dimensional stratified flow past a sphere. *J. Fluid Mech.* **192**, 393–419.

HANAZAKI, H., KONISHI, K. & OKAMURA, T. 2009 Schmidt-number effects on the flow past a sphere moving vertically in a stratified diffusive fluid. *Phys. Fluids* **21**, 026602.

JIANG, F., ZHAO, L., ANDERSSON, H.I., GUSTAVSSON, K., PUMIR, A. & MEHLIG, B. 2014 Inertial torque on a small spheroid in a stationary uniform flow. *Phys. Rev. Fluids* **6**, 024302.

JIANG, F., ZHAO, L., ANDERSSON, H.I., GUSTAVSSON, K., PUMIR, A. & MEHLIG, B. 2020 Inertial torque on a small spheroid in a stationary uniform flow. *Phys. Rev. Fluids* **6**, 024302.

KATIJA, K. & DABIRI, J.O. 2009 A viscosity-enhanced mechanism for biogenic ocean mixing. *Nature* **460** (7255), 624–626.

KHAYAT, R.E. & COX, R.G. 1989 Inertia effects on the motion of long slender bodies. *J. Fluid Mech.* **209**, 435–462.

KIM, S.J. & KARRILA, S. 1991 *Microhydrodynamics*. Dover.

KIORBOE, T. 2011 How zooplankton feed: mechanisms, traits and trade-offs. *Biol. Rev.* **86**, 311–339.

KUNZE, E., DOWER, J.F., BEVERIDGE, I., DEWEY, R. & BARTLETT, K.P. 2006 Observations of biologically generated turbulence in a coastal inlet. *Science* **313** (5794), 1768–1770.

KUSHCH, V.I. 1997 Microstresses and effective elastic moduli of a solid reinforced by periodically distributed spheroidal particles. *Intl J. Solids Struct.* **34** (11), 1353–1366.

KUSHCH, V.I. 1998 Elastic equilibrium of a medium containing a finite number of arbitrarily oriented spheroidal inclusions. *Intl J. Solids Struct.* **35** (12), 1187–1198.

LAB, K. 2018 *Phytoplankton Identification Guide 2018*. Blurb.

LEAL, L.G. 1992 *Laminar Flow and Convective Transport Processes*. Butterworth-Heinemann.

LIST, E.J. 1971 Laminar momentum jets in a stratified fluid. *J. Fluid Mech.* **45** (3), 561–574.

MARATH, N.K. & SUBRAMANIAN, G. 2017 The effect of inertia on the time period of rotation on an anisotropic particle in simple shear flow. *J. Fluid Mech.* **830**, 165–210.

MEHADDI, R., CANDELIER, F. & MEHLIG, B. 2018 Inertial drag on a sphere settling in a stratified fluid. *J. Fluid Mech.* **855**, 1074–1087.

MERCIER, M.J., WANG, S., PÉMÉJA, J., ERN, P. & ARDEKANI, A.M. 2020 Settling disks in a linearly stratified fluid. *J. Fluid Mech.* **885**, A2.

MROKOWSKA, M.M. 2018 Stratification-induced reorientation of disk settling through ambient density transition. *Sci. Rep.* **8**, 412.

MROKOWSKA, M.M. 2020*a* Dynamics of thin disk settling in two-layered fluid with density transition. *Acta Geophys.* **68**, 1145–1160.

MROKOWSKA, M.M. 2020*b* Influence of pycnocline on settling behavior of non-spherical particle and wake evolution. *Sci. Rep.* **10**, 20595.

MUNK, W.H. 1966 Abyssal recipes. *Deep Sea Res. Oceanogr. Abstr.* **13** (4), 707–730.

PAGE, M.A. & JOHNSON, E.R. 2008 On steady linear diffusion-driven flow. *J. Fluid Mech.* **606**, 433–443.

PATRICIA, E., FREDERIC, R., DAAUGUSTE, F., FABRE, D. & MAGNAUDET, J. 2012 Wake-induced oscillatory paths of bodies freely rising or falling in fluids. *Annu. Rev. Fluid Mech.* **44**, 97–121.

PHILLIPS, O.M. 1970 On flows induced by diffusion in a stably stratified fluid. *Deep-Sea Res.* **17**, 435–443.

PRAIRIE, J.C., ZIERVOGEL, K., CAMASSA, R., MCLAUGHLIN, R.M., WHITE, B.L., DEWALD, C. & ARNOSTI, C. 2015 Delayed settling of marine snow: effects of density gradient and particle properties, and implications for carbon cycling. *Mar. Chem.* **175**, 28–38.

ROBERTO, C., CLAUDIA, F., JOYCE, L., MCLAUGHLIN, R.M. & PARKER, R. 2009 Prolonged residence times for particles settling through stratified miscible fluids in the stokes regime. *Phys. Fluids* **21**, 031702.

SAFFMAN, P.G. 1965 The lift on a small sphere in a slow shear flow. *J. Fluid Mech.* **22** (2), 385–400.

SHAIK, V.A. & ARDEKANI, A.M. 2020 Far-field flow and drift due to particles and organisms in density-stratified fluids. *Phys. Rev.* E **102**, 063106.

SRDIC-MITROVIC, A.N., MOHAMED, N.A. & FERNANDO, H.J.S. 1999 Gravitational settling of particles thruogh density interfaces. *J. Fluid Mech.* **381**, 175–198.

SUBRAMANIAN, G. 2010 Viscosity-enhanced bio-mixing of the oceans. *Curr. Sci.* **98**, 1103–1108.

SUBRAMANIAN, G. & KOCH, D.L. 2005 Inertial effects on fiber motion in simple shear flow. *J. Fluid Mech.* **535**, 383–414.

TURNER, J.S. 1973 *Buoyancy Effects of Fluids*. Cambridge University Press.

TURNER, J.T. 2015 Zooplankton fecal pellets, marine snow, phytodetritus and the ocean's biological pump. *Prog. Oceanogr.* **130**, 205–248.

TURNER, A. & HOLMES, L. 2011 Occurrence, distribution and characteristics of beached plastic production pellets on the island of malta (central mediterranean). *Mar. Pollut. Bull.* **62**, 377–381.

VARANASI, A.K. & SUBRAMANIAN, G. 2021 Motion of a sphere in a viscous stratified fluid. arXiv:2107.14422

VISSER, A. 2007 Biomixing of the oceans? *Science* **316** (5826), 838–839.

WUNSCH, C. 1970 On oceanic boundary mixing. *Deep-Sea Res.* **17**, 293–301.

YICK, K.Y., TORRES, C.R., PEACOCK, T. & STOCKER, R. 2009 Enhanced drag of a sphere settling in a stratified fluid at small Reynolds numbers. *J. Fluid Mech.* **632**, 49–68.

ZVIRIN, Y. & CHADWICK, R.S. 1975 Settling of an axially symmetric body in a viscous stratified fluid. *Intl J. Multiphase Flow* **1**, 743–752.